Research Square

Preprints are preliminary reports that have not undergone peer review.
They should not be considered conclusive, used to inform clinical practice,
or referenced by the media as validated information.

MAH-g-PLA Compatibilization and ATBC Plasticization of Biodegradable PLA/PBAT Blends: A Combined Experimental and Molecular Dynamics Study

Hongtao Li
Lishan Kang
Letian Shi
Ni Tang
Mingjun Yang
myang@swpu.edu.cn

Southwest Petroleum University https://orcid.org/0000-0003-0551-2446

Research Article

Keywords:

Posted Date: November 3rd, 2026

DOI: https://doi.org/10.21203/rs.3.rs-11332121/v1

License: This work is licensed under a Creative Commons Attribution 4.0 International License.
Read Full License

MAH-g-PLA Compatibilization and ATBC Plasticization of Biodegradable PLA/PBAT Blends: A Combined Experimental and Molecular Dynamics Study

Hongtao Li[1], Lishan Kang[1], Letian Shi[1], Ni Tang[1], Mingjun Yang[1*]

[1*]School of New Energy and Materials, Southwest Petroleum University, Chengdu, 610500, P. R. China.

*Corresponding author(s). E-mail(s): myang@swpu.edu.cn;
Contributing authors: 202522000681@stu.swpu.edu.cn; 202422001307@stu.swpu.edu.cn; 202521000749@stu.swpu.edu.cn; 202522000700@stu.swpu.edu.cn;

Abstract

Polylactide/poly(butylene adipate-co-terephthalate) (PLA/PBAT) blends are central to biodegradable packaging. Reactive compatibilization with maleic-anhydride-grafted polylactide (MAH-g-PLA) and plasticization with acetyl tributyl citrate (ATBC) jointly toughen the 70/30 w/w blend; we resolve their combined molecular action by all-atom molecular dynamics on experimentally anchored formulations. Two Flory–Huggins χ routes straddle zero, bracketing a partial-miscibility window consistent with the two amorphous populations resolved by dynamic mechanical analysis (DMA). In the compatibilized blend the succinic-anhydride graft ring localizes on PBAT-rich regions (three-quarters of ring atoms within 0.5 nm of PBAT) while the PLA arm bridges towards PBAT (**1.13**× enrichment) — a polymeric surfactant consistent with the mechanical optima at 3–5 parts per hundred resin (phr). For the plasticizer, a Fox-equation mass balance of the DMA peak shifts and the simulated 0.5-nm contact statistics independently recover the same ordering: an interfacial/PBAT-associated sink fills first (≈98% of ATBC outside both phase bulks at 1 phr), and direct PLA-phase dissolution grows appreciably only near 5 phr (never exceeding 13% of molecules). At 1–3 phr ATBC anti-plasticizes by occupying free volume without

creating it (fractional free volume invariant across loadings and seeds), the structural signature of the experimental ductility minimum. These cross-validated descriptors provide design rules for balancing compatibilizer and plasticizer loadings in foamable PLA blends.

Keywords: PLA/PBAT blends, MAH-g-PLA, ATBC, molecular dynamics, biodegradable polymers, plasticization

1 Introduction

Polylactide (PLA) is the leading bio-based and industrially compostable polyester, yet its inherent brittleness (elongation at break below 10%) restricts use in packaging and cushioning applications. Blending with poly(butylene adipate-co-terephthalate) (PBAT), a flexible and fully biodegradable aliphatic–aromatic polyester, is the most economical route to toughened PLA-based materials [7, 33]. Uncompatibilized PLA/PBAT blends, however, form a two-phase sea–island morphology over most of the composition range, and their mechanical performance is limited by weak interfacial adhesion [33]. The same interfacial adhesion also governs cell morphology in CO_2-blown foams of this blend family [14, 36, 38], so quantifying its molecular-level origin serves both the solid blend and its foamed derivatives.

Whether PLA and PBAT are thermodynamically miscible remains actively debated. Solubility-parameter arguments and Flory–Huggins modelling predict miscibility windows at $M_n \approx 30$ kg/mol and near-ambient temperature [32], whereas experiment consistently resolves two glass transitions and phase-separated morphologies [33]. Multiscale simulation and experiments suggest that 50/50 mixtures exhibit the worst miscibility among common ratios [21], and copolymer compatibilizers analogous to PLA/PBAT block architectures improve miscibility [29, 40]. Molecular dynamics (MD) has been applied to PLA/PBAT with generic force fields: Zakizadeh et al. combined experiment with MD to characterize in-situ compatibilized blends [39]; gas diffusion in the same blend has been simulated with a class-II force-field platform [31]; Caputo et al. used server-generated OPLS-AA parameters for starch-reinforced PLA/PBAT blends [5]; and micro-cross-linked PBAT has been shown by MD to improve miscibility in poly(L-lactide) (PLLA) [37]. In all of these studies the PBAT intramolecular torsions rely on transferred or auto-generated parameters, and no dedicated first-principles parameterization of PBAT conformational energetics has been reported, let alone one whose adoption into production simulations was decided by a pre-registered gate; the state of molecular simulation of polymer blends is reviewed in [15].

Reactive compatibilization with maleic-anhydride-grafted PLA (MAH-g-PLA) is a practical route to stronger PLA/PBAT interfaces: the pendant anhydride groups can esterify with the hydroxyl and carboxyl chain ends of both polyesters during melt blending, while the PLA backbone of the graft interpenetrates with the matrix, so that loadings from a few phr (parts per hundred resin) upward refine the PBAT dispersed phase and raise the work of fracture [7, 24]. In parallel, acetyl tributyl citrate

(ATBC), a bio-based citrate ester, plasticizes the same blends: it lowers the glass-transition temperature (T_g) and the melt viscosity, improving the processability of PLA/PBAT blends [9]. In the experiments reported here, the full formulation matrix PLA/PBAT 70/30 + MAH-g-PLA (3–20 phr) + ATBC (1–5 phr) reveals optima at 3–5 phr MAH-g-PLA (impact versus elongation at break) and 4 phr ATBC (elongation 389%, recovering from an anti-plasticization window at 1–3 phr), tracked by melt flow rate (MFR), tensile and impact testing, differential scanning calorimetry (DSC) and dynamic mechanical analysis (DMA) glass transitions, thermogravimetric analysis (TGA), and scanning electron microscopy (SEM). Several molecular-level questions, however, cannot be answered by these macroscopic observations alone: how ATBC partitions between the PLA/PBAT interface and the phase bulks — indirectly accessible from DMA peak shifts through the Fox mixing rule [2, 9], but never confronted with a molecular picture — how the free volume responds across loadings, and how the grafted anhydride alters interfacial structure when the esterification chemistry itself is not directly observable.

This paper combines the experimental campaign with all-atom molecular dynamics on matched formulations. First, we assemble and validate a transferred OPLS-AA PBAT force field, and we confront it with a first-principles parameterization track — periodic density functional theory (DFT) of butylene-terephthalate, butylene-adipate, and junction fragments (van-der-Waals-corrected Perdew–Burke–Ernzerhof, PBE) feeding CHELPG charges and torsion profiles through a *pre-registered adoption gate* — which delivers a falsification-grade diagnosis of the force field's glass-transition excess: even the full DFT ester electrostatics leave the T_g overestimate largely intact, establishing that the excess is controlled by the packing/free-volume equation of state rather than by the ester electrostatics or torsion profiles tested here. Second, the additive molecules are parameterized on the same first-principles footing: the ATBC plasticizer and a succinic-anhydride-grafted PLA trimer (the covalent MAH-g-PLA graft point) receive DFT-derived CHELPG charges. Third, we use these force fields to quantify the structure, glass transition, and cohesive energetics of the 70/30 blend and of compatibilized/plasticized variants, confronting the simulated observables with the measured MFR, DSC/DMA, and SEM trends. Compared with the closest previous combined study [39], the present contribution differs in three respects: (i) a first-principles parameterization *track with a pre-registered adoption gate* that turns force-field shortcomings into a quantitative diagnosis, instead of a silently retained stock commercial force field; (ii) a cross-validated account of ATBC partitioning in which a Fox-equation mass balance of the DMA peak shifts and the explicit molecular contact statistics recover the same concentration ordering, rather than an inference from either alone; and (iii) an accounting of simulated T_g that is explicit about cooling rate, molecular weight, and *sampling depth* — including the explicit statement of what the protocol cannot resolve — which places the simulated and measured transition temperatures on a known footing [11].

2 Experimental and computational methods

2.1 Materials, compounding, and characterization

PLA (grade FY801) and PBAT (grade TH801T) were supplied by Laidi New Materials (Ningbo) Co., Ltd.; nominal datasheet values for these grades (manufacturer's data) are a density of 1.24 g/cm^3, a melt-flow rate of ≈4 g/10 min (190 °C, 2.16 kg) and a melting point of ≈170–175 °C for FY801, and a density of 1.21–1.22 g/cm^3, a melt-flow rate of ≈2.5–5 g/10 min (190 °C, 2.16 kg) and a melting point of ≈110–130 °C for TH801T; the molecular weights of the base resins were not supplied. The compatibilizer was a commercial maleic-anhydride-grafted PLA (MAH-g-PLA) with a supplier-stated grafting ratio of 1.2% (Dongguan Haobang Plastics, a plastics trader rather than the synthesizer; the grafting ratio is as provided by the supplier and was not independently verified), and the plasticizer was acetyl tributyl citrate (ATBC, 97%, catalogue T819551, Shanghai Macklin Biochemical Co., Ltd.).

Compounding and specimen preparation

PLA, PBAT, and MAH-g-PLA were vacuum-dried at 80 °C for 12 h and melt blended in a three-zone internal mixer (140/175/180 °C, 60 rpm, 10 min), followed by injection moulding at 180 °C into dumbbell tensile and bar specimens. The base formulation was PLA/PBAT 70/30 (w/w). The compatibilized series PBM(x) added $x = 3, 5, 10, 15, 20$ phr of MAH-g-PLA; the plasticized series PBM-A(x) was based on PBM5 and added x = 1–5 phr of ATBC. The molecular model represents the graft chain as a PLA 20-mer carrying one succinic-anhydride ring; relative to the supplier-stated 1.2% grafting ratio (roughly one ring per 110 backbone units) this oligomer-scale model over-represents the grafting density by a factor of about five, an idealization propagated as a documented limitation.

Differential scanning calorimetry

DSC (Mettler–Toledo, STARe software v10.00; sample masses 5.18–7.34 mg, standard aluminium crucibles, N_2 purge 50 mL/min) covered all eleven formulations with a heat–cool–reheat program between 20 and 200 °C at 10 °C/min in all segments (second heating reported); because the 20 °C lower bound of the DSC scans lies above the PBAT-phase glass transition, the evidence for the PBAT transition comes from DMA. Glass transition, cold-crystallization, and melting data are quoted from the instrument analysis, cross-checked against an independent tangent re-analysis of the raw curves; the degree of crystallinity (X_c) was evaluated from the melting enthalpy against the literature reference enthalpy of 100% crystalline PLA, $\Delta H_f^0 = 93.6$ J/g [10].

Dynamic mechanical analysis

DMA (TA Instruments DMA850, 35 mm dual-cantilever clamp; bar specimens ≈35 × 10 × 4 mm) resolved the storage/loss moduli and tan δ of PBM5 and PBM-A1–A5 from −60 to +128 °C at 3.0 °C/min and 1 Hz, with a measured oscillatory strain of ≈0.058% (20 μm displacement). For the phase-resolved plasticizer balance of Section 3.4, tan δ peak positions were refitted parabolically over ±3 K windows (fit uncertainty combined with a 0.3 K assignment systematic).

Thermogravimetric analysis

TGA (Mettler–Toledo, STARe; sample masses 2.6–15.3 mg, 25–600 °C at 10 °C/min under N_2, 50 mL/min) covered both series plus neat PLA.

Melt flow, tensile, and impact testing

Melt flow was measured following GB/T 3682.1 at 190 °C under 2.16 kg with five replicates per formulation in the MAH-g-PLA series and single runs in the ATBC series (0.37–0.88 g/10 min across both series); tensile properties (strength and elongation at break) were measured following GB/T 1040.2 on type 1BA dumbbell specimens at a crosshead speed of 50 mm/min, and impact strength following GB/T 1043.1 on notched Charpy bars (type A notch), with three replicates each (mean ± standard deviation reported).

Scanning electron microscopy

Fracture surfaces were sputter-coated with gold and imaged by SEM (Zeiss EVO MA15, 10 kV) at 500× and 1000×.

Key anchors for the simulations: blend T_g = 58.6 °C and X_c = 23.3%; PBM5 T_g = 67.3 °C; PBM-A1–A5 T_g = 41–44 °C (ATBC plasticization $\Delta T_g \approx -25$ K relative to PBM5); DMA β peaks at −19 to −23 °C and α peaks at 62–67 °C.

2.2 Force fields

PLA was described by PLAFF3 [23], an OPLS-AA-based parameterization in which the ester torsions are refitted to ab initio scans; the published GROMACS topology workflow was used, with the tabulated torsion potential rebuilt as an explicit Fourier (function type 9) series fitted to the tabulated potential (RMS 0.69 kJ/mol) after detecting an inconsistency between the energy and force columns of the distributed table.

PBAT was assembled on the OPLS-AA skeleton [16] as a random butylene-terephthalate/butylene-adipate (BT/BA) copolymer (44/56 mol%, assumed as a typical ecoflex-class composition): all bonds, angles, and proper dihedrals are enumerated explicitly by a chain-builder script, with atom types from the standard ester set (opls_465–468). Five aromatic-ester torsions and one angle absent from the stock distribution were patched from benzylic-ester analogues (`pbat_estertypes.itp`); a DFT-derived replacement of these terms was tested at the pre-registered gate of Section 2.3 and not adopted. Chain ends are free hydroxyls (butanediol –OH termini, opls_154/157 atom types), the V0 lever reference sharing this topology; methyl-ester capping was tested as lever V1 ($\Delta T_g \approx +4$ K relative to V0) and does not reverse any trend. The 1–4 interactions are treated uniformly along the whole force-field line: the force field generates 1–4 pairs automatically with the standard OPLS-AA scaling (genpairs, fudgeLJ = fudgeQQ = 0.5), so the automatically generated PBAT 1–4 pairs are physically equivalent to the explicit [pairs] lists carried by the PLA chains, the difference being one of input format only. The resulting description reproduces the PBAT melt density to −2% (Table 1). This 1–4 degree of freedom was nevertheless probed directly in the lever study: scaling the 1–4 Lennard-Jones and Coulomb terms globally

(variants V7–V9 of Table 2) densifies the melt and raises T_g without reversing any trend, and the interfacial conclusions of this paper (the term is operationally defined in Section 2.5) rest on enrichment ratios and contact fractions between like-treated groups, which are insensitive to the 1–4 scaling.

2.3 DFT parameterization track (Track B) and its scope

Three PBAT fragments — the BT dimer, the BA dimer, and the BT–BA junction trimer — together with the two additive molecules of Section 2.4 were treated with a common first-principles protocol in VASP [18, 19] using PBE–D3 [13, 27] (projector-augmented-wave method with the standard PAW-PBE datasets, plane-wave cut-off 500 eV, Γ-point-only sampling of the large molecular cells, Gaussian smearing of 0.05 eV): reference geometries built with RDKit/ETKDG and MMFF94s and pre-relaxed with GFN2-xTB (bond-graph connectivity verified before every submission), PREC=Accurate relaxation with IBRION=2 (force criterion 0.001 eV/Å where reachable; 0.01 eV/Å accepted as the electrostatic-potential (ESP) fitting standard where the FFT-grid noise floor dominates; restart files are always purged between precision levels), and CHELPG charges [3] fitted to the LVHAR electrostatic potential sampled on cubic shells 0.4–2.8 Å beyond the molecular van-der-Waals (vdW) surface (0.3 Å spacing, trilinear interpolation, nearest-image correction, charge-constrained least squares after removal of the periodic reference constant); the five molecules close with relative RMS residuals of 0.09–0.16. Fragment torsion profiles follow the torsion-refitting practice of Robertson et al. [30]; the parent ester parameters are the LOPLS-AA set [28], whose ester torsions are the parents of the stock OPLS-AA ester types (opls_465–468) used in the production topology, so the scanned fragments map one-to-one onto the production parameter set.

The scope of this track in the present paper is deliberately limited and stated explicitly: the two *additive* models (ATBC and the MAH graft point) use their CHELPG charges directly in the production simulations. The *PBAT* production force field, by contrast, is the transferred OPLS-AA ester set with standard OPLS charges throughout; the coarse fragment torsion profiles constitute a staged reparameterization whose incorporation was tested on the pure melt at a pre-registered adoption gate: quick-screen T_g = 340.9 K versus 360.2 K for the transferred parameter set (Section 3.1, Table 2; all T_g values quoted to 0.1 K for traceability to the per-run fit reports), a 19.3 K improvement that falls short of the pre-registered 40 K threshold. The gate variant inherits the free-hydroxyl backbone of the V0 reference; against the topologically matched free-hydroxyl V0 (360.2 K) the recovery is 19.3 K, whereas against the methyl-ester-capped V1 (364.5 K) it would be 23.6 K — the gate conclusion is unchanged under either reference. The gate therefore closes on the transferred-parameter branch, and no blend or compatibilized simulation of this paper uses the reparameterized set.

2.4 DFT parameterization of the additive molecules

The ATBC plasticizer and a model of the MAH-g-PLA graft point receive the same first-principles treatment as the PBAT fragments. The graft model (mahgpla3) is an MeO-/OH-capped PLA trimer whose central methine hydrogen is replaced by

a succinic-anhydride ring ($C_{14}H_{18}O_{10}$), i.e. the covalent product of radical MAH grafting onto the PLA backbone; ATBC is taken in its entirety ($C_{20}H_{34}O_8$). Both molecules closed the full pipeline (connectivity-verified GFN2-xTB start geometries, vdW-corrected PBE re-optimization, CHELPG/LVHAR charges with relative RMS residuals of 0.16 for ATBC and 0.09 for the graft model). CHELPG charges of buried atoms are individually ill-conditioned — a known pathology that affects the central quaternary carbon of ATBC — but the fitted sets were audited for this, and the partitioning conclusions below rest on geometric contact statistics rather than on any individual charge. Lennard-Jones and bonded (bond, angle, torsion) parameters are transferred from the OPLS-AA ester/ether set, which covers all atom types present in both molecules; the ATBC liquid density at 298 K validates to −4.0% against experiment (Table 1).

2.5 Blend construction

The 70/30 (w/w) blend contains 32 PLA 40-mers (2.9 kDa) and 11 PBAT chains of 17 diacid repeat units (BT/BA 44/56 mol% nominal, realized as 8:9 per 17-unit chain, 3.7 kDa), 17,226 atoms total (69.8 wt% PLA), packed with PACKMOL [22] at low density and compressed during equilibration. Pure-component reference systems (40 PLA 40-mers; 30-chain PBAT melt, ∼15 k atoms) were built analogously. The equilibrated cubic box edge (5.8 nm) is marginally larger than twice the component radius of gyration ($R_g \approx 2.9$ nm): chain self-image interactions through the periodic boundary are therefore not fully eliminated, a finite-size regime shared by oligomeric melt simulations generally; the ratio-based interfacial and partition observables of Sections 3.5–3.6 are constructed to be insensitive to this bias (and were verified robust across velocity seeds), while absolute single-chain statistics (R_g, persistence length) retain the associated uncertainty. Two scale consequences are stated explicitly because they bound every localization claim below. First, at this box scale no macroscopic phase boundary is resolvable: the blend is a molecularly interdigitated mixture whose inter-chain radial distribution functions (RDFs) are featureless beyond the first solvation shell (Section 3.2), so "interfacial" is used throughout in a strictly operational, local sense — a molecule or group whose atoms contact both PLA and PBAT material within 0.5 nm — denoting a local molecular environment, not a resolved planar interface. Second, the transferred PBAT parameterization overestimates the neat-PBAT glass transition by ≈101 K against experiment (Table 1); the DFT reparameterization track (Section 2.3) attributes this excess to the packing equation of state rather than to the tested electrostatics/torsions, so all localization and partition conclusions are stated on shift-invariant observables only.

Compatibilized and plasticized variants matched to the experimental formulations are built with the same protocol: the B1 box adds four MAH-g-PLA graft chains (PLA-20 with one succinic-anhydride ring, ≈4.5 wt%, i.e. 4.7 phr on the base-resin mass, 17,994 atoms; Fig. 1), and the B2 series inserts 4, 7, 13, and 17 ATBC molecules on top of the B1 box (1.2, 2.1, 3.9, and 5.1 phr; 18,242–19,048 atoms), with phr converted on the base-resin mass basis, $\text{phr} = 100\, m_{\text{additive}}/(m_{\text{PLA}} + m_{\text{PBAT}})$. Graft chains enter packing as coil-relaxed conformers (0.5 ns pre-equilibration at a 0.5 fs time step, 1×10^6 steps); isobaric–isothermal (NPT) equilibration used a two-stage

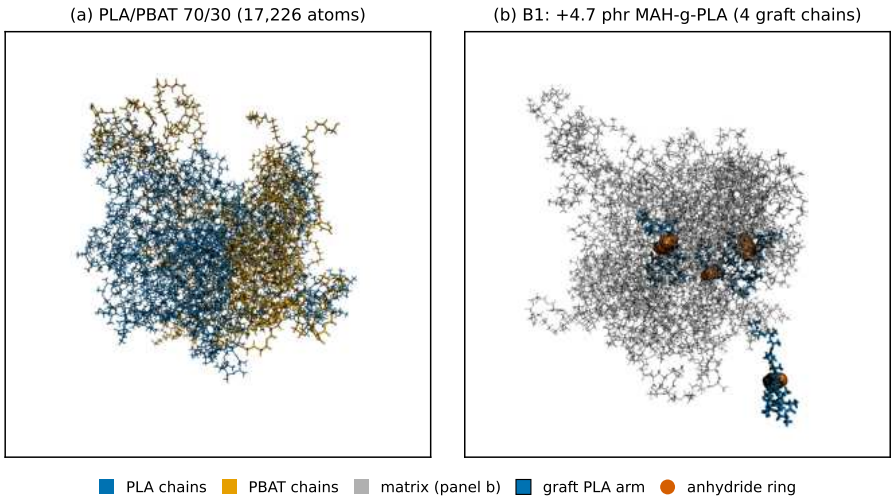


Fig. 1 Atomistic models of the simulated systems, rendered with VMD/Tachyon from the final 450 K NPT configurations. (a) Uncompatibilized 70/30 PLA/PBAT blend: 32 PLA 40-mers (blue) and 11 PBAT chains (orange), 17,226 atoms, 5.8-nm cubic box. (b) Compatibilized B1 blend (4.7 phr MAH-g-PLA): matrix chains grey; the four graft chains are highlighted, each a PLA 20-mer arm (blue) carrying one succinic-anhydride ring (vermilion) that anchors the graft at PLA–PBAT contacts.

Berendsen compression (500 ps at 2000 bar, 500 ps at 1 bar) after slow Parrinello–Rahman compression, which was found necessary to close packing voids from the low-density PACKMOL start. Service-state observables were obtained from 10-ns NPT continuations at 300 K started from the 300 K configurations of the cooling scans; these continuations cover the four boxes from 0 to 3.9 phr (B1 and the 1.2, 2.1, and 3.9 phr ATBC boxes), the 5.1 phr box having no 300 K continuation.

2.6 Simulation protocol

All simulations used GROMACS 2026.3 [1] (standard mixed precision; key energies cross-checked against a double-precision build, AVX-512). After steepest-descent energy minimization (EM), systems were brought to 450 K by a 0.2 ns NVT (constant-volume, constant-temperature) run (1 fs step, velocities initialized at 450 K) and equilibrated under NPT (constant-pressure, constant-temperature; isotropic Parrinello–Rahman barostat [26], $\tau_p = 5.0$ ps, compressibility 4.5×10^{-5} bar^{-1}) with the stochastic velocity-rescaling thermostat [4] ($\tau_t = 0.1$ ps). Production runs at 450 K used particle-mesh Ewald (PME) electrostatics (1.0 nm real-space cut-off, default $\approx$0.12 nm Fourier grid spacing), Lennard-Jones interactions truncated at 1.0 nm with a long-range dispersion correction applied to the energy and pressure, the LINCS (Linear Constraint Solver) algorithm constraining X–H bonds, and a 2 fs time step; the blend was sampled for 10 ns.

Glass transitions were located by cooling from the 450 K equilibrated melt in 25 K steps (1 ns per step, 425–200 K, $\tau_t = 0.5$ ps, $\tau_p = 2.0$ ps), averaging the density over the last 0.5 ns of each step and fitting the specific volume with two-segment

(single-kink) and three-segment (dual-kink) linear models under the model-selection criteria of Section 2.7. The protocol follows the reproducibility guidelines of Carmona Esteva et al. [6]. A strict slow-cooling protocol (10 K steps, 3 ns each, 3.3 K/ns) was used to quantify the cooling-rate artifact. Oligomeric T_g values are corrected for molecular weight using Fox–Flory scaling [11] ($T_g(\infty) = 333$ K and $K \approx 1.1 \times 10^5$ K g/mol, typical literature values for PLA, applied to the PLA control); for PBAT the same scaling (taking the literature bulk value $T_g(\infty) = 248$ K) places the 3.7 kDa oligomer expectation at ≈218 K, so quoting the bulk experimental range in Table 1 is conservative — the molecular-weight-corrected excess is larger still.

2.7 Structural analysis

Inter-component RDFs were computed between PLA ester oxygens (O1/O4) and PBAT ester oxygens, and between carbonyl carbons, over the last 5 ns of production, with both GROMACS `rdf` (group-name selections) and MDAnalysis (topology from coordinate files). Radii of gyration were evaluated per component; agreement between the two analysis paths is within 0.1 nm. Backbone persistence lengths were obtained from tangent–tangent correlations of virtual bonds (every second backbone heavy atom) along unwrapped chains, $C(k) = \langle t_i \cdot t_{i+k} \rangle \propto \exp(-k\langle l_v \rangle / \ell_p)$, averaged over the last half of each production trajectory; fractional free volume (FFV) was measured by Monte Carlo probe insertion with probe radius zero (2×10^5 seeded random trial points per frame against vdW-radii-excluded spheres, minimum-image distances; C 1.70, O 1.52, H 1.20 Å), averaged over 26 frames spanning the last 5 ns of each production trajectory (13 frames over the last 2.5 ns for the shorter pure-PLA run) with one identical protocol for every box of Sections 3.2–3.6 so that the graft and plasticizer series are internally comparable. Widom test-particle insertion [35] had been the planned primary route to the plasticizer chemical potential, but insertion acceptance is expected to converge poorly in dense, quenched matrices of this kind, and the analysis was therefore downgraded a priori to the contact and partition statistics reported in Section 3.6. For that partitioning analysis, each ATBC molecule is classified per frame by the share of its heavy atoms within 0.5 nm (minimum-image convention) of PBAT and of PLA backbone carbons (graft chains excluded from the PLA group): *PBAT-anchored* when more than 50% contact PBAT, *interfacial* when more than 20% contact PBAT and more than 20% contact the PLA backbone, and *PLA-dissolved* when more than 50% contact the PLA backbone and at most 20% contact PBAT. These classes are not mutually exclusive by construction — an anchored molecule usually also satisfies the interfacial criterion — so population shares need not sum to 100%. Statistical uncertainties of the cohesive-energy and χ analyses were quantified by block averaging (four 1.25 ns blocks of the last 5 ns).

Glass transitions are obtained from piecewise-linear fits of the specific volume $v(T)$ over the ten 1-ns cooling points plus the production 450 K anchor. Single-kink (glass slope constrained below melt slope) and dual-kink models are scanned over all admissible splits; the dual-kink solution is accepted only when both kinks fall inside the data range and reduce the residual sum of squares by at least 20%, otherwise the single-kink value is reported. In view of the broad transitions the kink positions carry a fit-choice bandwidth of 10–15 K, estimated from the spread of accepted kink

Table 1 Pure-component and additive validation of the assembled force fields (production set: transferred OPLS-AA ester parameters with standard charges for PBAT; CHELPG charges for ATBC and the graft model)

Quantity	Model	Experiment[c]	Deviation
ρ PLA melt (450 K, kg/m^3)	1150	1120–1130	+1.8–2.7%
ρ PBAT melt (450 K, kg/m^3)	1110	≈1130	−1.8%
ρ ATBC liquid (298 K, kg/m^3)	1004	1046	−4.0%
T_g PLA 40-mer (K)	302.2	≈295[a]	+7 K
T_g PBAT 17-mer (K)	344.4	238–243[b]	+101 K
CHELPG relative RMS residual (5 DFT molecules)	0.09–0.16	—	—

[a] Fox–Flory expectation for the 2.9 kDa oligomer; the bulk experimental value is 328–333 K. [b] Bulk experimental range; the +101 K excess is a force-field free-volume effect, not a protocol or molecular-weight artifact (PLAFF3 control passes at +7 K; no classical lever in Table 2 lowers it, and the DFT-gate variant V11 recovers only 19 K). [c] Experimental anchors are typical literature ranges [33].

positions as the split point is scanned over the admissible range of each fit; the run-to-run spread of the extracted kink across velocity seeds is larger still, ±40 K (pooled standard deviation across the six replicate fits; Section 3.6), so this protocol does not report T_g trends across loadings. Key interfacial and partition observables were therefore additionally repeated with independent velocity seeds (two additional seeds each for B1 and the 2.1 phr box, three runs total), and run-to-run standard deviations are quoted alongside those values.

3 Results and discussion

3.1 Force-field validation: melt density and glass transition

Table 1 summarizes the pure-component validation against experimental anchors.

The PLA control experiment validates the entire cooling/fitting protocol: the raw T_g of 2.9 kDa PLA 40-mers (302 K) lies within 7 K of the Fox–Flory expectation for that molecular weight, indicating that the 25 K/ns cooling schedule and bilinear fit introduce a systematic bias within 7 K [11]. For PBAT the strict slow-cooling scan (3.3 K/ns) yields 344 K, about 100 K above the experimental 238–243 K [33]; an independent MD study of the same polymer yields 280 K for PBAT [31], +37 K above the same experimental range; the present +101 K excess is nearly three times as large. A ten-variant sensitivity study (Table 2: torsional softening and hardening, 1–4 Lennard-Jones and charge scaling, hydroxyl-to-ester capping, dispersion scaling) shows that *every* lever that softens the torsion space either leaves the density trend unchanged or raises T_g further: the simulated transition is controlled by packing/free-volume, and softer chains densify (counter-intuitively) increasing the glass point. The ≈1.3 percentage-point (≈3% relative) free-volume deficit of PBAT relative to PLA (Section 3.2) is directionally consistent with a higher glass point on free-volume (Doolittle/Williams–Landel–Ferry-type) scaling, but cannot account for the full +101 K, i.e. the free-volume equation of state itself differs between the two parameter sets. Parameter-level tuning of the transferred torsions is therefore exhausted. The staged Track-B reparameterization of Section 2.3 was applied to the

Table 2 PBAT T_g lever study (6k-atom screening protocol: EM, NVT 450 K, 3 ns NPT, 425–200 K cooling at 25 K per 1 ns; single-seed bilinear fits; absolute kink positions carry the sensitivity documented in Section 3.6). "—" = density threshold failed. No classical lever lowers T_g: torsion-space changes (softening, zeroing, or hardening) densify the melt and raise T_g, while end-capping and dispersion scaling lower the density without lowering T_g; the V11 row is the DFT charge/torsion gate variant, which densifies yet recovers 19 K. Densities of these 6k-atom screening boxes mostly run below the 15k-atom production systems of Table 1 (finite-size effect); V11 densifies through its DFT charges and is the exception. Differences between levers are of the same order as the seed noise documented in Section 3.6 and are read as a directional scan; T_g values are quoted to 0.1 K for traceability to the fit reports

Variant	Modification	ρ_{450} (kg/m^3)	T_g (K)
V0	reference (free OH ends, transferred aryl-ester)	1081	360.2
V1	OH ends → methyl-ester capped	1072	364.5
V2	V1 + aryl-ester torsion softened	1100	399.1
V3	V1 + all ester torsions zeroed (diagnostic)	1101	387.9
V4	V2 + all $\varepsilon \times 0.9$	1062	394.0
V5	V2 + all $\varepsilon \times 0.8$	1029	—
V6	V2 + CT/HC $\varepsilon \times 0.9$	1083	387.4
V7	fudgeQQ 0.25	1087	381.5
V8	fudgeQQ 0.0	1097	391.0
V9	fudgeLJ 0.0	1093	382.1
V10	ester torsions hardened to DFT shape (func-9)	1100	391.4
V11	DFT fragment CHELPG + coarse torsion fits	1112	340.9

pure melt at the pre-registered gate — DFT fragment CHELPG charges (ester polarity $+0.59/-0.42$ versus the OPLS $+0.51/-0.33$) plus the three coarse torsion fits — and yielded $T_g = 340.9$ K in the same quick-screen protocol (Table 2, V11 row): a 19 K improvement that — assuming the recovery transfers to the strict slow-cooling protocol (the quick-screen versus strict-scan offset is 16 K, 360.2 versus 344.4 K) — would leave an $\approx +82$ K excess over experiment. The full first-principles ester electrostatics therefore move the glass point in the right direction without curing it, which closes the diagnosis: the excess is controlled by the packing/free-volume equation of state of the transferred nonbonded parameter set rather than by the ester force constants or charges. This paper accordingly reports blend transitions in a *relative-offset* framework (cooling-rate and Fox–Flory corrections stated explicitly) rather than as absolute predictions.

3.2 70/30 blend: density, glass transition, and structure

The blend density increases from 1147 kg/m^3 (450 K) to 1230 kg/m^3 (200 K) on cooling; the compatibilized boxes track this curve point-by-point within $\approx$6 kg/m^3

and are themselves seed-reproducible to the same tolerance (Section 3.6). The single-kink fit of the specific volume (Fig. 2) gives T_g = 342.7 K (69.5 °C); the dual-kink alternative is degenerate (both kinks fall in the same 348–356 K window with negligible residual-sum-of-squares (RSS) improvement), i.e. the two component transitions merge into one broad transition under the current PBAT parameterization, consistent with the compressed — in fact inverted — component T_g gap of the force field (PBAT 42 K *above* PLA, 344 versus 302 K, against 88 K *below* in experiment, 243 versus 331 K). Experimentally, PLA/PBAT blends retain two separate glass transitions at all compositions studied [25, 33], so the single simulated transition must be read as a force-field artifact of the compressed component gap rather than evidence of full miscibility; the relative-offset framework of Section 3.1 applies, and the kink position itself carries the fit-choice sensitivity documented in Section 3.6 (the argument rests on the merger of the two transitions, not on the exact kink temperature). The present formulations are no exception to the experimental rule: every DMA-characterized formulation (PBM5, PBM-A1–A5) exhibits a PBAT-rich β relaxation beside the PLA-phase α peak — two coexisting glass transitions constituting the two-phase evidence developed in Section 3.4, precisely the partially miscible, two-phase picture in which a single simulated transition must be interpreted.

Structurally, the inter-component RDFs are featureless (Fig. 3): the ester–oxygen cross-correlation ($\mathrm{PLA_{ester\,O}}$–$\mathrm{PBAT_{ester\,O}}$) rises monotonically from its first non-zero value at ∼2.5 Å towards unity ($g \approx 0.2$ at 0.35 nm, $g \approx 0.85$ at 1.0 nm, approaching one only beyond ∼1.5 nm) without a first-shell peak, and the carbonyl-carbon cross-RDF ($\mathrm{PLA}_{C=O}$–$\mathrm{PBAT}_{C=O}$) behaves likewise, with first contacts at ∼3.3 Å. By contrast, the like–like PBAT–PBAT self-correlation overshoots unity in the same range ($g \approx 2.0$ at 0.5 nm) while remaining as featureless and monotone as the cross-correlations: the like–like correlation runs well above the cross-correlations throughout, qualitatively consistent with mild like-species enrichment against depleted hetero-contacts (the like–like curve contains intramolecular contributions, so this comparison is qualitative) and, in either reading, with the absence of specific attractive interactions between the two components (there are no hydrogen-bond donors on either backbone) and compatibility governed by dispersion and packing. Component radii of gyration are $R_g = 2.86 \pm 0.01$ nm (PLA) and 2.89 ± 0.01 nm (PBAT), reproduced to within 0.1 nm by two independent analysis implementations. Backbone persistence lengths in the melt at 450 K are ℓ_p = 3.3 Å (PLA, ℓ_K = 6.6 Å) and 3.8 Å (PBAT, ℓ_K = 7.6 Å), i.e. both components are similarly flexible at this temperature, and the fractional free volumes are 44.8% (PLA), 43.5% (PBAT), and 43.8% (blend, 26 frames over the last 5 ns (13 frames over the last 2.5 ns for the shorter pure-PLA run), one identical seeded-insertion protocol across all systems of this work): PBAT packs denser than PLA under the present force field, in line with the free-volume interpretation of its overestimated glass point (Section 3.1).

3.3 Cohesive energies and the Flory–Huggins parameter

Intermolecular cohesive energies were isolated from the total nonbonded energy by subtracting single-chain (intramolecular) contributions evaluated under an identical cut-off rerun protocol, so that periodic self-image terms cancel exactly. The resulting

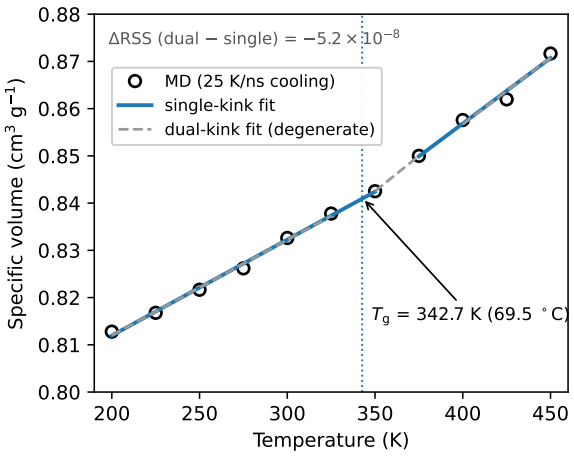


Fig. 2 Specific volume of the 70/30 blend versus temperature with the single-kink fit ($T_g = 342.7$ K); the dual-kink alternative is degenerate (both kinks in the same 348–356 K window; the annotated ΔRSS (dual − single) $= -5.2 \times 10^{-8}$ is the residual-sum-of-squares change of the dual-kink over the single-kink fit, which is negligible), i.e. the two component transitions merge into one broad transition under the present force field. Kink positions carry a run-to-run sensitivity of ±40 K (Section 3.6)

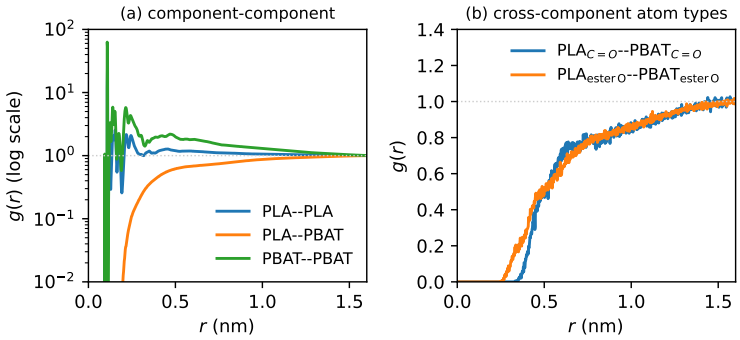


Fig. 3 Blend structural analysis. (a) Whole-component RDFs (PLA–PLA, PLA–PBAT, PBAT–PBAT) on a logarithmic scale; the sharp peaks below ∼0.2 nm (e.g. PLA–PLA $g = 36.6$) are intramolecular bonded (1–2) contributions. (b) Cross-component atom-type correlations (carbonyl carbons PLA$_{C=O}$–PBAT$_{C=O}$ and ester oxygens PLA$_{\text{ester O}}$–PBAT$_{\text{ester O}}$; `gmx rdf`, bin width 0.002 nm, last 5 ns of the production trajectory): the featureless monotone rise indicates compatibility governed by dispersion and packing rather than specific interactions

Hildebrand parameters at 450 K are $\delta_{\text{PLA}} = 16.93 \pm 0.16$ and $\delta_{\text{PBAT}} = 17.79 \pm 0.18$ MPa$^{1/2}$ (standard errors from 1.25 ns block averages): the absolute values sit ∼15% below the literature estimates (19.9–21.3 and 20.0–23.2 MPa$^{1/2}$ [32, 33]), a systematic effect of the short-range cut-off protocol (no dispersion tail, no long-range electrostatics); because the same cut-off physics acts on both components, the *difference* $\Delta\delta$ is partially error-cancelling, and the resulting χ is best read as a lower bound

on magnitude. The *ordering* $\delta_{\mathrm{PBAT}} > \delta_{\mathrm{PLA}}$ and their small difference ($\Delta\delta = 0.9$ $\mathrm{MPa}^{1/2}$) reproduce the experimental trend. The Hildebrand estimate of the Flory–Huggins parameter, $\chi = V_{\mathrm{ref}}(\Delta\delta)^2/RT$ evaluated per block and averaged (so that block-to-block variance of δ raises the mean above the value obtained by substituting the average $\Delta\delta$), is small and positive, $+0.014 \pm 0.006$ to $+0.024 \pm 0.010$ for reference volumes of 58.1 and 100 $\mathrm{cm}^3/\mathrm{mol}$ (the PLA repeat-unit molar volume and a generic lattice-site choice, respectively; Fig. 4) — borderline immiscibility, consistent with the two-phase morphologies and double glass transitions seen experimentally [25, 33], and with the present measurements (dual tan δ peaks whose PBAT-rich component is shifted upward, overlapping two-step degradation in TGA, and a two-phase morphology inferred from the mechanical and melt-flow response, with the SEM fractographs providing qualitative support; Section 3.4). A positive entropic contribution of the same magnitude is expected from backbone-stiffness mismatch [12, 17, 34]; mapping our melt persistence lengths onto the bead–spring calibration of Kozuch et al. gives $\chi_s \approx 3 \times 10^{-4}$ per segment, small here because both chains are similarly flexible at 450 K, but strictly positive and therefore reinforcing the borderline-immiscible picture rather than cancelling it.

In contrast, the energy-of-mixing route applied to the 70/30 blend (Figs. 4 and 5), $B = \Delta e/(\phi_A\phi_B) = -196 \pm 34$ MPa ($\chi = -3.0 \pm 0.5$ at $V_{\mathrm{ref}} = 58.1$ $\mathrm{cm}^3/\mathrm{mol}$), indicates favorable hetero-contacts, echoing the theoretical prediction of thermodynamic miscibility at $M_n \approx 30$ kg/mol [32]. The block analysis, however, reveals a systematic drift of B across the four consecutive blocks ($-261 \to -246 \to -155 \to -120$ MPa): the mixing energy has not converged within 10 ns, so the large negative χ must be regarded as a lower bound on magnitude rather than an equilibrated estimate, and the apparent conflict with the (stable, positive) Hildebrand route is most parsimoniously attributed to incomplete equilibration of the single composition rather than to strongly attractive hetero-contacts. Both routes therefore bracket the long-standing PLA/PBAT miscibility debate (theoretically compatible, practically phase-separated), with the block-converged Hildebrand estimate — small positive χ, reinforced by the entropic stiffness term — as the more defensible of the two; a multi-composition mixing-energy series would be needed to equilibrate this route and is left for future work.

3.4 Experimental characterization: processing, mechanical, and thermal response

Melt flow decreases with MAH-g-PLA loading (Fig. 6) — MFR = 0.57, 0.47, 0.48, 0.37, 0.42 g/10 min at 3, 5, 10, 15, 20 phr (the uncompatibilized blend was not characterized for melt flow; the ATBC series below is therefore referenced to PBM5) — consistent with anhydride–hydroxyl esterification raising the melt viscosity, with a minimum at 15 phr and a slight recovery at 20 phr. ATBC raises the melt flow monotonically above the PBM5 reference: 0.70, 0.74, 0.74, 0.75, 0.88 g/10 min at 1–5 phr, all well above PBM5 (0.47).

Tensile data separate the two series cleanly (Fig. 7). In the PBM series, elongation at break peaks at 5 phr (254%, versus 65% for the uncompatibilized blend) and decreases to 106% at 20 phr, while strength holds at 23.6–24.1 MPa up to 5 phr before

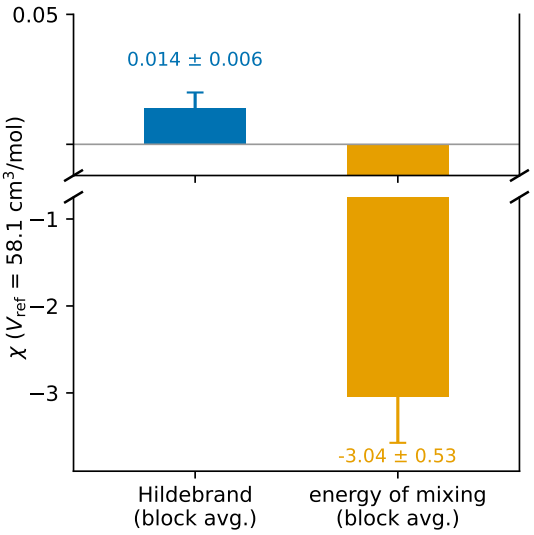


Fig. 4 Block-averaged Flory–Huggins parameter from the two cohesive-energy routes: Hildebrand solubility parameters (stable, small positive, $+0.014 \pm 0.006$, upper segment of the broken axis) and the blend mixing energy ($V_{\mathrm{ref}} = 58.1$ cm^3/mol)

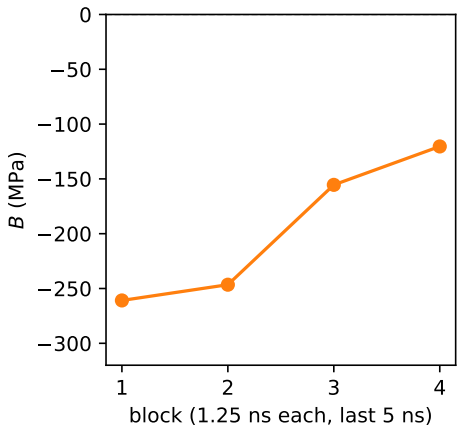


Fig. 5 Energy-of-mixing interaction parameter B per block: the systematic drift shows the mixing-energy route is not equilibrated within 10 ns and its negative χ is a lower bound

decreasing to 19.6 MPa at 20 phr; impact toughness peaks early, at 3 phr (28.0 kJ/m^2). In the PBM-A series the salient feature is the *anti-plasticization* window: at 1–3 phr ATBC the elongation at break (125–178%) remains well below the PBM5 reference (254%) and impact drops to 13.7–14.3 kJ/m^2 (versus 23.6), before ductility recovers sharply at 4–5 phr (389% and 382%; impact peak 17.3 kJ/m^2 at 4 phr). Strength decreases mildly from 25.8 to 20.9 MPa across the series.

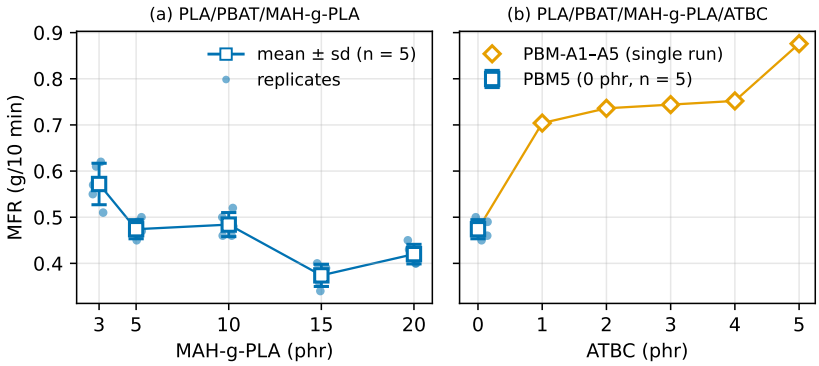


Fig. 6 Melt flow rate versus (a) MAH-g-PLA and (b) ATBC loading. In (a), five raw replicates per composition are shown as jittered points with mean ± sd (open squares, $n = 5$). In (b), PBM5 (5 phr MAH-g-PLA, no ATBC) anchors the series at $x = 0$ with its five replicates ($n = 5$); the PBM-A1–A5 (single run) points are open diamonds ($n = 1$). The compatibilizer raises melt viscosity (esterification), the plasticizer raises the melt flow back monotonically above the PBM5 anchor

The toughening gains carry a strength penalty that must be stated plainly. The uncompatibilized blend is the strongest material of the campaign (34.2 MPa), and every compatibilized formulation falls to 24.1 MPa or below, the plasticized series to 25.8 MPa or below — a 25–31% reduction relative to the 34.2 MPa matrix against which the impact and ductility gains (28.0 kJ/m^2 at 3 phr, 254% at 5 phr) are purchased. The PBM-A series sits at 20.9–25.8 MPa, i.e. the plasticizer does not recover the strength either. The design window is therefore a trade-off, not a uniform improvement, and the compatibilizer/plasticizer loadings identified below should be read as balancing toughness against this strength floor.

Thermally, the DSC second heating (Fig. 8) gives blend $T_g = 58.6$ °C and $X_c = 23.3\%$; MAH-g-PLA first suppresses crystallinity (X_c drops to 10.2% at 3 phr) before heterogeneous nucleation partly recovers it ($X_c \approx 20\%$ at 5 phr, falling back to 18.3, 17.8, and 13.9% at 10, 15, and 20 phr), and T_g rises to 67.3 °C at 5 phr (settling at 65.1, 63.4, and 65.5 °C at 10, 15, and 20 phr). ATBC suppresses the PLA-phase glass transition strongly, dropping ≈23 K already at 1 phr and levelling at 41–44 °C ($\Delta T_g \approx -25$ K relative to PBM5 across 1–5 phr), the primary plasticization anchor for the simulations of Section 3.6. TGA (Figs. 9 and 10) shows $T_{5\%} = 318$–344 °C and single-to-double derivative thermogravimetric (DTG, $-dm/dT$) maxima (369–383 °C); PBM-A4 resolves two overlapping DTG steps and records the lowest $T_{5\%}$ of the campaign (317.7 °C) — consistent with a partly phase-separated structure in which the second, earlier degradation step reflects an ATBC-rich phase losing mass ahead of the matrix. DMA (Fig. 11) delivers the key compatibility evidence: every DMA-characterized formulation (PBM5, PBM-A1–A5) shows two tan δ peaks, a PBAT-rich β relaxation at −19 to −23 °C — ∼5–10 K above the neat-PBAT glass transition of −28 to −30 °C measured by DSC [33], an offset to which the expected DMA-versus-DSC frequency shift contributes, so the two coexisting peaks, not the offset magnitude, carry the two-phase evidence — and a PLA-phase α relaxation at 62–67 °C that

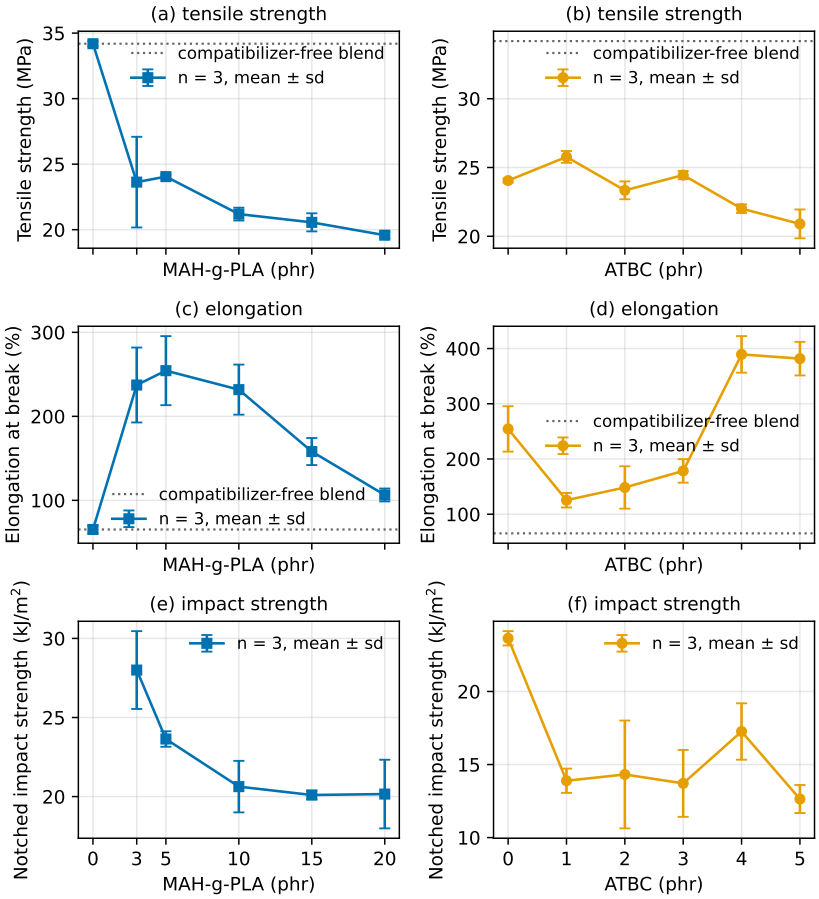


Fig. 7 Mechanical properties ($n = 3$, mean ± sd). Left column, MAH-g-PLA series (0–20 phr, PLA/PBAT at $x = 0$); right column, ATBC series (0–5 phr, PBM5 at $x = 0$). (a,b) tensile strength, (c,d) elongation at break, (e,f) impact strength. The grey dotted baseline marks the uncompatibilized PLA/PBAT blend (34.19 MPa tensile strength, 65.3% elongation at break); its impact strength was not measured, so panel (e) starts at PBM3. The PBM-A anti-plasticization window (1–3 phr) and the 4–5 phr ductility recovery bracket the plasticizer optimum

ATBC shifts downward monotonically: by only −0.2 K at 1 phr and by ≈ −5 K at 5 phr (DMA tan δ, 1 Hz), versus ≈ −25 K by DSC.

The peak shifts also support a quantitative, phase-resolved plasticizer balance through the Fox mixing rule [2, 8, 9] (Fig. 12). Taking the unplasticized compatibilized blend PBM5 as the reference state of each phase and $T_g(\mathrm{ATBC}) = 193$ K [2], the relation $w_{\mathrm{ATBC}} = (T_g^{-1} - T_{g,0}^{-1}) \,/\, (T_g(\mathrm{ATBC})^{-1} - T_{g,0}^{-1})$ converts each tan δ peak position into the plasticizer content of the corresponding phase. With the peak positions refitted parabolically and the uncertainty budget propagated (0.3 K assignment systematic plus the 185–205 K literature spread of $T_g(\mathrm{ATBC})$), neither phase bulk dissolves much plasticizer: the PLA-rich phase carries ≈0.0 wt% ATBC at 1 phr and only ≈2.0 wt%

at 5 phr, and the PBAT-rich phase ≈2.8 wt% at 5 phr; at 1 phr the β peak even lies above the PBM5 baseline, i.e. no measurable bulk plasticization of either phase at the lowest loading. Closed over the phase masses (PLA-rich : PBAT-rich = 75 : 30 per 105 g of the PBM5 blend, i.e. 70 g PLA + 30 g PBAT + 5 g MAH-g-PLA with the graft chains counted in the PLA-rich phase), the balance assigns the great majority of the added ATBC to an interfacial/excess population — point estimate 98% at 1 phr (lower bound ≈65% from the propagated uncertainty), 79% at 2 phr, and 46–52% at 4–5 phr (Fig. 12b). The same inversion applied to the DSC midpoint of the PLA phase (41–44 °C across the series) would require ≈10 wt% ATBC uniformly dissolved in the PLA phase — more ATBC than the formulation contains below 4 phr — so the calorimetric transition is carried by a plasticizer-saturated PLA sub-population that grows in extent with loading at near-constant concentration, while the DMA peaks track the majority domains.

SEM (Fig. 13; 1000×) contrasts the smooth, brittle fracture surface of neat PLA with the compatibilized/plasticized PBM-A series, showing cavitation-hole coarsening from PBM-A1 to PBM-A3, the most uniform fine porosity at PBM-A4, and ATBC over-saturation pores with sharp phase boundaries at PBM-A5. The experimental anchors confronting the simulations below are collected in Table 3.

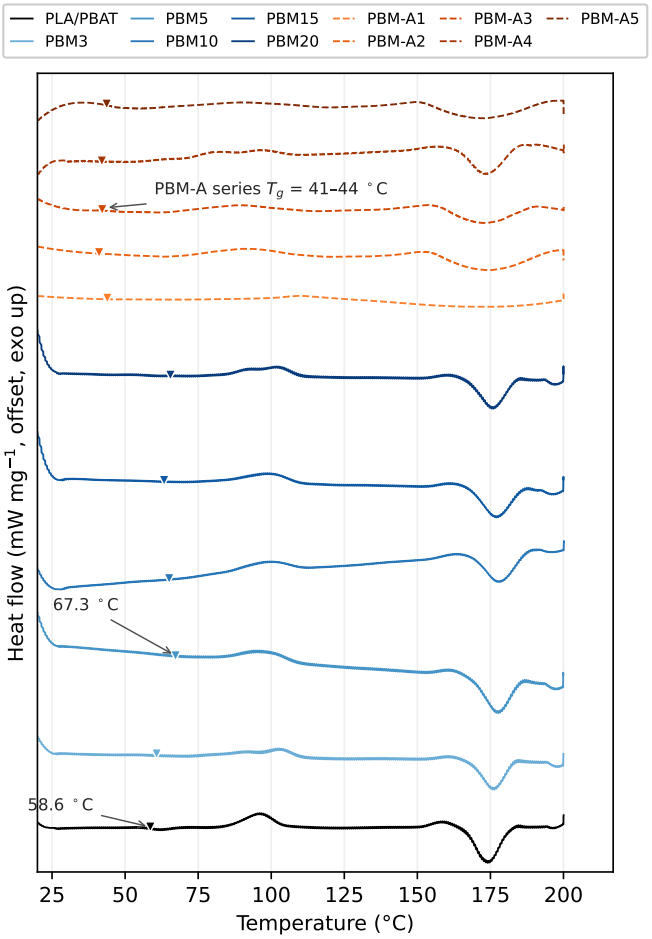


Fig. 8 DSC second-heating curves (10 °C/min) of the eleven formulations, normalized by sample mass (mW mg^{-1}), smoothed with a Savitzky–Golay filter (window ∼8 K), and stacked with a fixed vertical offset; exotherm direction is up. Triangles mark the reported T_g of each sample; arrows annotate 58.6 °C (PLA/PBAT), 67.3 °C (PBM5), and the 41–44 °C PBM-A series. The PLA-phase glass transition and the cold-crystallization/melting envelope track the compatibilizer and plasticizer loadings

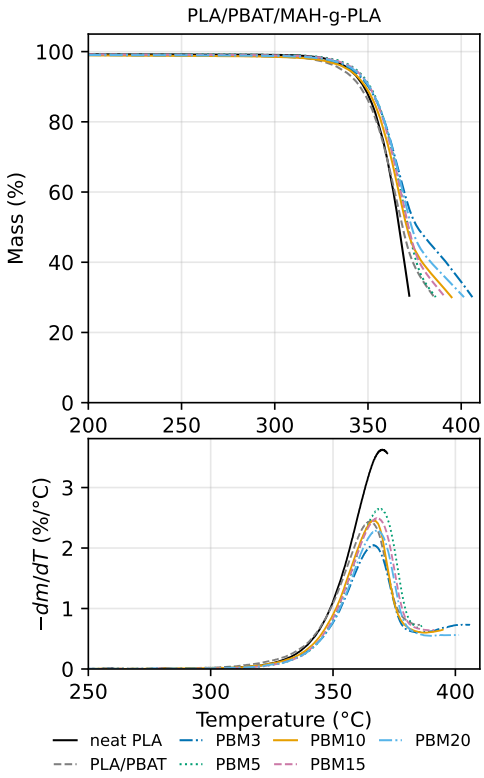


Fig. 9 TGA mass-loss curves (200–410 °C) of the MAH-g-PLA series (neat PLA, PLA/PBAT, PBM3–PBM20) with the DTG ($-dm/dT$) panel below

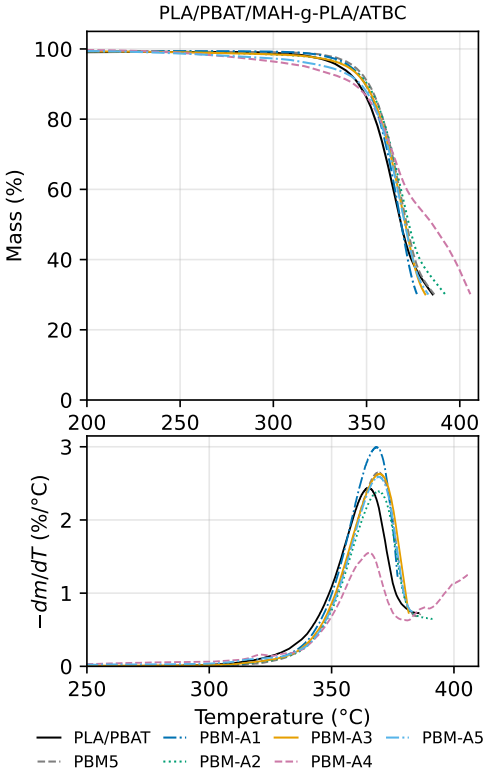


Fig. 10 TGA of the ATBC series (PLA/PBAT, PBM5, PBM-A1–A5) with the DTG panel below: the DTG maximum splits from single to double with formulation complexity — PBM-A4 resolves two overlapping degradation steps and shows the campaign-lowest $T_{5\%}$ (317.7 °C), consistent with an ATBC-rich phase losing mass ahead of the matrix

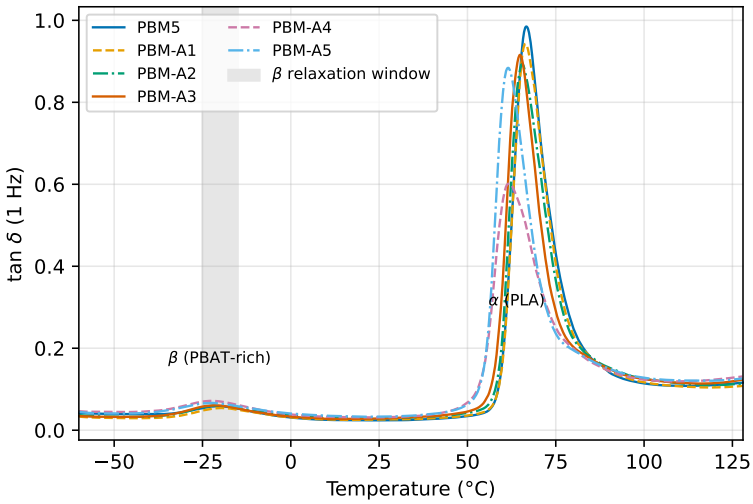


Fig. 11 DMA tan δ of PBM5 and the PBM-A series (1 Hz): PBAT-rich β relaxation (-19 to -23 °C, ∼5–10 K above the neat-PBAT glass transition of -28 to -30 °C measured by DSC [33], an offset partly due to the DMA-versus-DSC frequency shift; the grey band marks this β-relaxation window) beside the PLA-phase α peak (62–67 °C, shifted down monotonically by ATBC) — the partial-miscibility and plasticization evidence confronted by the simulations of Section 3.6

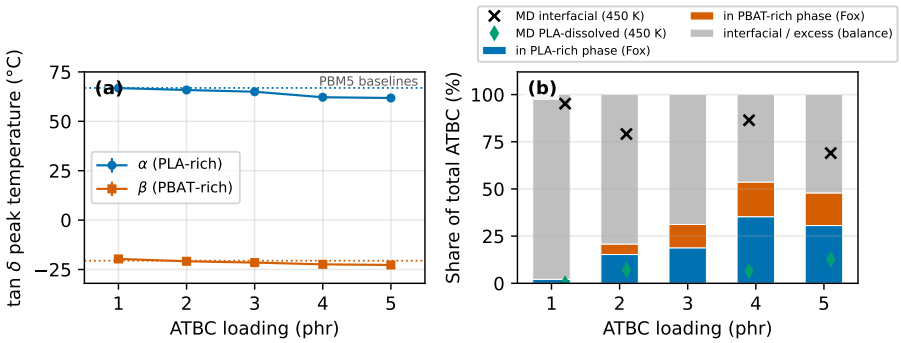


Fig. 12 Fox-equation inversion of the DMA peak shifts of Fig. 11 into a phase-resolved ATBC mass balance [2, 8, 9]. (a) tan δ peak temperatures of the PLA-rich (α) and PBAT-rich (β) phases versus ATBC loading (PBM5 baselines dotted; error bars combine the parabolic peak-refit uncertainty with a 0.3 K assignment systematic). (b) Share of the total added ATBC assigned to the PLA-rich and PBAT-rich phase bulks (Fox inversion, PBM5 reference state, T_g(ATBC) = 193 K) and to the interfacial/excess population by difference (bars), confronted with the MD contact-state populations of Section 3.6 (markers: interfacial and PLA-dissolved molecule fractions at 450 K, placed at the simulated loadings 1.2, 2.1, 3.9, and 5.1 phr)

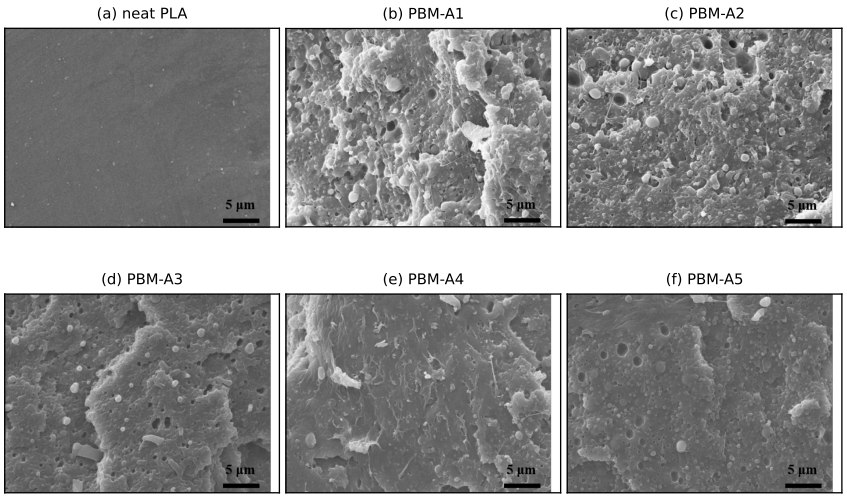


Fig. 13 SEM fracture-surface montage (1000×, 5 μm bars, all panels at identical magnification): (a) neat PLA and (b)–(f) PBM-A1–A5. Neat PLA fractures smooth and brittle; in the PBM-A series cavitation holes coarsen through the anti-plasticization window (A1–A3), turn into the finest uniform porosity at A4, and give way to over-saturation pores with sharp phase boundaries at A5

3.5 MAH-g-PLA localization between PLA and PBAT environments

The compatibilized system B1 adds four MAH-g-PLA graft chains (PLA-20 with one succinic-anhydride ring on the residue-10 methine, 4.5 wt%, 17,994 atoms) to the 70/30 baseline box and follows the identical protocol (crush–release NPT compression, 10 ns PME production at 450 K, 1 ns per cooling point). The production density, 1143 ± 8 kg/m^3 at 450 K, matches the baseline blend (1147 kg/m^3) within 0.4%, and the cooling curve is likewise featureless apart from a broad transition (single-kink $T_g = 314$ K versus 343 K for the baseline under the same fit); in view of the seed pathology documented in Section 3.6 ($\pm$40 K spread of the extracted kink across replicates of identical density curves), this 29 K shift is not resolved, and only the interfacial observables below are interpreted quantitatively.

The graft rings are unambiguously localized at PLA–PBAT contact regions (Fig. 14; "interfacial" here and below in the operational local sense defined in Section 2.5). Across the main run and two independent velocity seeds, the ring–PBAT radial distribution function exceeds the ring–PLA backbone correlation throughout the first nanometer (0.4–0.8 nm shell enrichment 1.2–4.6, conservative lower bound 1.2); on average 75.8 ± 1.6% of the ring atoms lie within 0.5 nm of a PBAT atom, versus 25.8 ± 13.6% for the PLA backbone carbons (seed ranges 74–77% and 12–39%). This preference is chemically consistent with the polar, aromatic ester character of the PBAT terephthalate unit interacting with the anhydride carbonyls. The PLA arm of the graft chain is dragged towards the interface as well: 62.8 ± 1.0% of graft-chain backbone carbons contact PBAT within 0.5 nm, a 1.13$\times$ enrichment over the pure PLA40 chains (55.5 ± 1.3%) of the same box. Taken together, the molecule behaves as a graft-block surfactant — anhydride anchor in PBAT, polyester arm in PLA — which is the microscopic counterpart of the experimental picture: the impact maximum at 3 phr and the elongation maximum at 5 phr (Section 3.4), with the MFR minimum at 15 phr marking the over-dosage regime, point indirectly to an optimal interfacial coverage in this loading window, above which the excess compatibilizer no longer finds interfacial area to occupy.

Table 3 Experimental anchors used by the simulations of Sections 3.5 and 3.6 (measured in this section).[a]

Quantity	Value	Simulation use
Blend T_g, PLA phase (DSC)	58.6 °C	Section 3.2 offset check
PBM5 T_g (DSC)	67.3 °C	Section 3.5 context
ATBC ΔT_g (1–5 phr)	≈ -25 K	Section 3.6 (beyond MD resolving power)
DMA β peak (PBAT-rich)	−19–−23 °C	Section 3.6 partitioning
DMA α peak	61.6–66.7 °C	Section 3.6 trend
E' at 25 °C	1.5–1.7 GPa	context only
X_c (blend / PBM5)	23.3% / 20.1%	discussion only
MFR minimum (15 phr)	0.37 g/10 min	Section 3.5

[a]The anti-plasticization window (PBM-A1–A3 ductility and impact below PBM5) is the experimental counterpart of the mechanism discussed in Section 3.6.

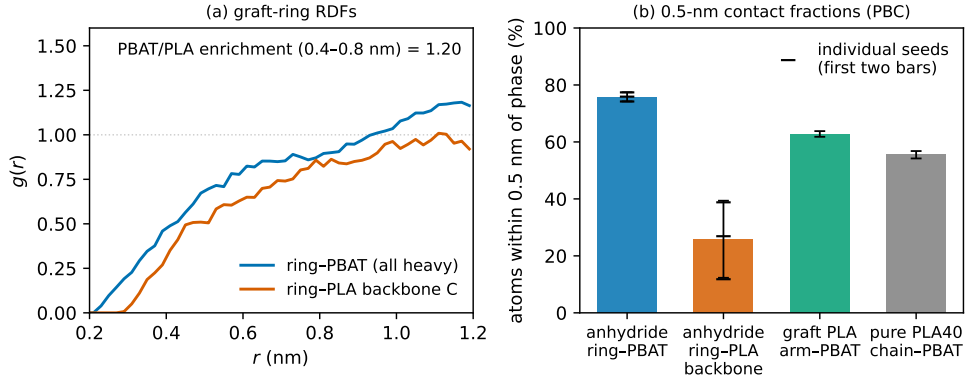


Fig. 14 MAH-g-PLA localization in the B1 blend (last 5 ns of the 10 ns production). (a) Graft-ring RDFs against PBAT (all heavy atoms) and PLA backbone carbons; the PBAT/PLA enrichment over the 0.4–0.8 nm shell is 1.2 for the main run (lower bound; up to 4.6 across velocity seeds), showing the anhydride ring anchored at PBAT-rich regions. (b) Fractions of atoms within 0.5 nm of the indicated phase: ring–PBAT 75.8 ± 1.6% and ring–PLA backbone 25.8 ± 13.6% (mean ± sd over the main run and two velocity seeds; tick marks show the individual seeds, corresponding to the 74–77% and 12–39% ranges quoted in the text), graft-chain PLA arm–PBAT 62.8 ± 1.0%, and pure PLA40 chain–PBAT 55.5 ± 1.3% (main box only; ± from frame-to-frame statistics within the run). The ring contacts PBAT nearly three times as often as the PLA backbone, and graft-chain PLA arms are enriched 1.13× over pure PLA40 chains — the bridging signature of a polymeric surfactant

3.6 ATBC partitioning, free volume, and T_g suppression

Four B2 boxes add 4, 7, 13, and 17 ATBC molecules (1.2, 2.1, 3.9, and 5.1 phr; 18,242–19,048 atoms) to the B1 formulation under the identical protocol. Production densities at 450 K are 1147 ± 6, 1145 ± 5, 1141 ± 6, and 1139 ± 6 kg/m^3: the 1.2 phr value is statistically indistinguishable from the B1 reference (1143 ± 8), and the density then

decreases monotonically with plasticizer loading, as expected for a diluent of lower density than the matrix.

The plasticizer is not randomly dispersed (Fig. 15). At the lowest loading essentially every ATBC molecule occupies a mixed local environment: 100% of molecules keep more than half their atoms within 0.5 nm of PBAT and 95% simultaneously keep a sizeable (>20%) share of their atoms near the PLA backbone — the operational interfacial contact state — with atom-level contact fractions of 91% (PBAT) versus 48% (PLA). Figure 16 shows a representative single-frame configuration of the 5.1-phr box with every ATBC molecule colored by this contact-state classification. At 2.1 phr this interfacial contact state saturates (79% of molecules — the contact classes are not mutually exclusive, an anchored molecule can also be interfacial — with the PBAT-anchored share at 42% and a 7% PLA-dissolved population appearing), and at 3.9 phr the excess redistributes back towards PBAT-rich regions (82% PBAT-anchored, interfacial 86%). At 5.1 phr — the experimental anchor loading of the −25 K ΔT_g — the PLA-dissolved population roughly doubles (12.7%, from 6.5–7.1% below) while the interfacial population recedes to 69%: the interfacial and PBAT contact sinks are now saturated, and the plasticizer finally reaches the PLA phase whose glass transition the DSC/DMA measurements track. Direct dissolution in the PLA phase never exceeds 13% of molecules. The MD thus arbitrates the two experimental threads of Section 3.4 in favor of a mixed picture — strong enrichment at PLA–PBAT contacts (SEM/impact evidence) with PBAT-rich regions as the only bulk sink (DMA β-peak evidence) — and predicts limited direct plasticization of the PLA phase, which only appears once the interfacial and PBAT sinks are saturated; the same concentration ordering is recovered independently by the Fox-equation mass balance of the DMA peak shifts (Fig. 12b).

The fractional free volume is strictly constant across the low-loading half of the series (43.8–43.9% at 450 K, 26 frames over the last 5 ns of each trajectory with seeded Monte Carlo insertion, one identical protocol across all boxes; the uncompatibilized 70/30 blend also sits at 43.8%): ATBC fills pre-existing free-volume pockets rather than creating new ones, the textbook condition for anti-plasticization — small-molecule occupation of unrelaxed volume that immobilizes neighbouring chain segments without lowering the overall density. Even at the two highest loadings the FFV rises only marginally (43.9–44.0% at 3.9 and 5.1 phr, +0.1–0.2 percentage points, comparable to the seed-to-seed noise of ±0.15 percentage points): the free volume is constant across the full series to within 0.2 percentage points. The high-loading onset nevertheless tracks the growth of the PLA-dissolved plasticizer population (which first appears at 2.1 phr): once the interfacial and PBAT sinks are saturated, the excess plasticizer begins to create free volume rather than occupy it — the molecular counterpart of the experimental over-saturation pores at PBM-A5 and of the 4–5 phr ductility recovery (Section 3.4). The invariants survive quenching to the service state: 10-ns continuations at 300 K give FFV = 41.0–41.2% across the 0–3.9 phr boxes with the ATBC partition pattern essentially unchanged (89.3/52.7/71.0% PBAT-contact at 1.2/2.1/3.9 phr, versus 91/51/68% at 450 K), i.e. the plasticizer distribution is an equilibrated structural feature, not a frozen kinetic accident of the melt. The

plasticizer mobility is consistent with this picture: the ATBC center-of-mass diffusivity in the 2.1 phr melt, estimated from the mean-squared displacement over the 10-ns trajectories, is 2.5×10^{-7} cm^2/s at 450 K — the order expected for a small molecule in a polymer melt — and falls by a factor of $\sim$27 on quenching to 300 K (9.3×10^{-9} cm^2/s), i.e. the pore-filling plasticizer is immobilized in the service state. Velocity-seed replicates of B1 and of the 2.1 phr box reproduce both the density cooling curves point-by-point to within $\approx$6 kg/m^3 and the FFV to within $\pm$0.15 percentage points, so these structural observables are robust. The simulated glass transition itself, by contrast, cannot be resolved with meaningful uncertainty under the present protocol: the transition is broad (glass-to-melt specific-volume slope ratio $\approx$1.8 only), and piecewise-linear fits — whether single- or dual-kink or local-slope midpoints — locate the transition anywhere between 314 and 425 K depending on split choice and velocity seed (run-to-run spread $\pm$40 K, exceeding any loading effect). The experimental T_g shift of -25 K at 5 phr (Section 3.4) is therefore outside the resolving power of 1-ns-per-point cooling scans of these boxes, and the anti-plasticization picture is argued here from the *structural* side — invariant FFV, interfacial/PBAT partitioning with a PLA-depleted plasticizer population — in combination with the experimental mechanics, not from simulated transition temperatures.

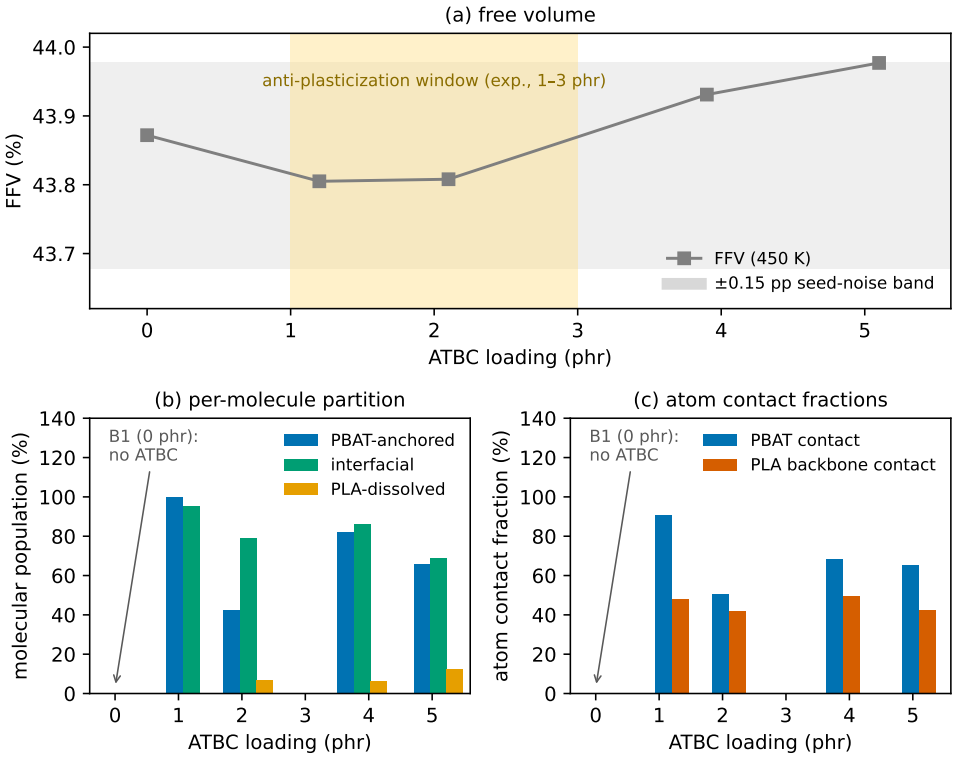


Fig. 15 ATBC plasticization of the compatibilized blend versus ATBC loading (nominal loadings 1.2, 2.1, 3.9, and 5.1 phr; no 3 phr box); $x = 0$ is the B1 box (compatibilized, no ATBC). (a) Fractional free volume (seeded insertion, 26 frames over the last 5 ns, one protocol across all boxes; the uncompatibilized 70/30 blend also sits at 43.8%); the grey band is the ±0.15-percentage-point seed-noise reference centred on the low-loading plateau, within which FFV is invariant through 2.1 phr — pore filling, not pore creation; the yellow band marks the experimental anti-plasticization window (1–3 phr) of Section 3.4. (b) Per-molecule ATBC populations (grouped bars): PBAT-anchored, interfacial, and PLA-dissolved; the PLA-dissolved population is zero at 1.2 phr, first becomes positive at 2.1 phr (7.1%), stays at 6.5–7.1% through 3.9 phr, and reaches 12.7% at 5.1 phr, only once the interfacial and PBAT sinks saturate. (c) Atom-level contact fractions (ATBC heavy atoms within 0.5 nm of PBAT and of the PLA backbone) — a distinct quantity from the molecular populations of (b). Together with the experimental mechanics these structural observables carry the anti-plasticization argument; simulated transition temperatures are not resolvable at this sampling depth (see text)

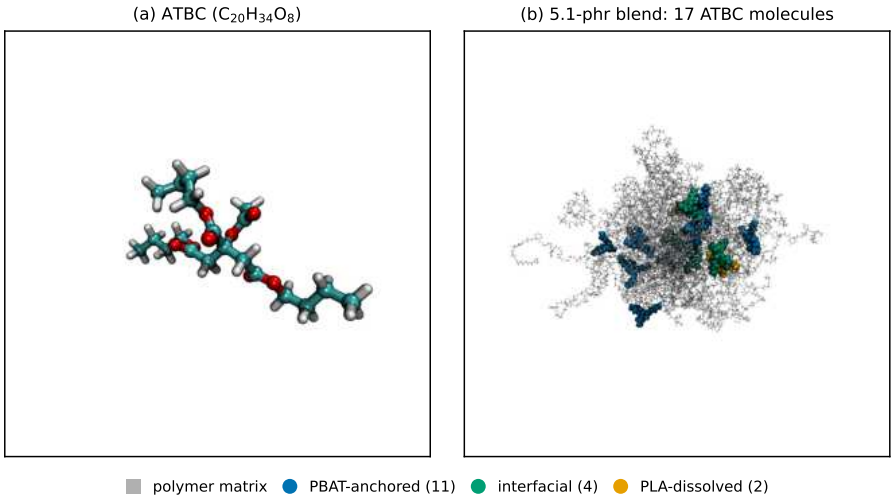


Fig. 16 ATBC plasticizer geometry and partitioning (VMD/Tachyon). (a) Acetyl tri-*n*-butyl citrate ($C_{20}H_{34}O_8$, 62 atoms, ball-and-stick with element colors: carbon teal, oxygen red, hydrogen white). (b) The 5.1-phr compatibilized blend (final 450 K NPT configuration, matrix grey): each of the 17 ATBC molecules is colored by its single-frame 0.5-nm contact state using the same contact criteria as Fig. 15b with an exclusive single-frame assignment (anchored > interfacial > dissolved) — PBAT-anchored (blue, 11 molecules), interfacial (green, 4), and PLA-dissolved (orange, 2); the trajectory-averaged populations are given in Fig. 15

4 Discussion and conclusions

Reactive versus physical compatibilization

One boundary of the present model must be drawn sharply. The experimental MAH-g-PLA mechanism is *reactive*: pendant anhydride rings esterify polyester chain ends during melt processing, so part of the compatibilizer population ends up covalently grafted to PBAT (and, secondarily, to PLA). The simulation models only the *physical* state — pre-formed MAH-g-PLA molecules acting as non-reactive graft-block surfactants — because classical MD cannot follow the esterification chemistry. The interfacial-anchoring and bridging picture of Section 3.5 therefore constitutes the physical component of the compatibilization free energy; the reactive component (covalent PBAT-g-PLA junctions, lower interfacial energy still, and viscosity build-up consistent with the MFR trend) acts on top of it. The two mechanisms are complementary rather than competing, and the consistency of the physical picture with the experimental 3–5 phr optima suggests that coverage of the interface by amphiphilic graft chains — rather than the number of covalent links alone — sets the performance window.

Localization mechanism of MAH-g-PLA

The molecular picture that emerges from Sections 3.5 and 3.6 is that of a two-level microstructure: the compatibilizer decorates the PLA/PBAT interface, and the plasticizer in turn populates the interface decorated by the compatibilizer. The graft chains behave as polymeric surfactants — anhydride anchors in contact with PBAT-rich regions (ring–PBAT RDF enrichment 1.2–4.6× across seeds, contact probability 74–77% versus 12–39% for PLA) with the PLA arm enriched 1.13× towards PBAT over pure PLA40 chains. At 5 phr loading this interfacial film is far from saturated, which is consistent with the experimental optimum lying at 3–5 phr: below it the interface is only partially covered (impact maximum at 3 phr), while the MFR minimum at 15 phr and the decline of both impact strength and elongation beyond 3–5 phr indicate that excess compatibilizer eventually acts as a separate, poorly dispersed phase rather than finding further interface. The non-reactive classical model cannot follow the anhydride–hydroxyl esterification itself — the graft is represented as a pre-formed covalent product — but the MFR viscosity rise and the interfacial activity are two faces of the same chemistry, and the simulation supplies the missing structural link between them.

Anti-plasticization as pore filling

The ATBC series demonstrates the classic small-molecule anti-plasticization mechanism in atomistic detail: the fractional free volume is strictly constant up to 2.1 phr (43.8–43.9%) — the plasticizer occupies pre-existing free-volume pockets and immobilizes the surrounding segments. FFV rises only marginally ($\leq$0.2 percentage points, comparable to the seed-to-seed noise of $\pm$0.15 percentage points) at the higher loadings where the PLA-dissolved population grows, until interfacial saturation flips the mechanism to genuine pore creation at 5 phr, mirroring the SEM over-saturation pores. The experimental signatures align: the 1–3 phr window of depressed ductility

and impact, and the DMA β peak of the PBAT-rich population (shifted ∼5–10 K above the neat-PBAT glass transition at −28 to −30 °C [33]), which drifts downward weakly but monotonically by ≈3.5 K across A1–A5, consistent with progressive plasticization of the PBAT-rich phase; the larger shift is carried by the PLA-phase α peak (66.7 → 61.6 °C). The Fox-equation balance of these shifts quantifies the same trend (Fig. 12, developed below). Three caveats bound the agreement. First, the broadness of the simulated transition (glass-to-melt slope ratio ≈1.8) makes any T_g extraction from 1-ns-per-point cooling scans unstable across velocity seeds (±40 K spread), so the simulated T_g response to ATBC is reported as unresolved rather than compared point-by-point with the experimental −25 K at 5 phr; resolving it would require longer per-temperature sampling or larger boxes. Second, ATBC partitions almost exclusively to the interface and PBAT-rich regions (≤13% of molecules dissolve in PLA, and only after the interfacial sink saturates: ≤7.1% up to 3.9 phr, rising to 12.7% at 5.1 phr), so a simulated blend-level transition — were it resolvable — would be dominated by the interfacial and PBAT-segment populations (the populations that carry the experimental β-relaxation), whereas the experimental α-peak reflects the PLA phase, which the MD predicts to be nearly ATBC-free. Third, the structural invariants themselves (density curves to ≈6 kg/m^3, FFV to ±0.15 percentage points, partition populations) are robust across seeds and carry the anti-plasticization argument as presented.

The Fox inversion of the DMA shifts (Fig. 12) turns this apparent experiment–simulation mismatch into a quantitative reconciliation. The calorimetric PLA-phase transition is carried by a plasticizer-saturated sub-population (≈10 wt% ATBC by the same mixing rule) — an interphase that saturates from the first phr and then grows in extent rather than in concentration — while the DMA α peak tracks the majority PLA domains, whose plasticizer content reaches only ≈2 wt% at 5 phr. The DMA-based mass balance places ≈98% of the added ATBC outside either phase bulk at 1 phr and still 46–52% at 4–5 phr, the same concentration ordering as the MD contact-state populations (95% interfacial — i.e. contacting PBAT — at 1.2 phr, falling to 69% at 5.1 phr as the PLA-dissolved minority grows to 12.7%). The thermal baseline is consistent with such an interface-localized mechanism: MAH-g-PLA itself raises the blend T_g by +8.7 K (58.6 → 67.3 °C at 5 phr compatibilizer, PBM5), i.e. the compatibilizer stiffens the interface region it decorates, and a plasticizer partitioning preferentially into that stiffened interphase can produce the large-magnitude, rapidly saturating apparent ΔT_g seen by DSC. The two operational definitions differ — the Fox residual is a mass-balance quantity, the MD classification a 0.5-nm geometric contact state — so the absolute percentages are not expected to coincide, and both mix genuine interphase material with plasticizer loosely associated to domain boundaries; the contact-based counting in particular bounds rather than measures true PLA-phase dissolution, since an ATBC molecule dissolved in a PLA-rich region that still touches a PBAT atom within 0.5 nm is classified as interfacial. What the comparison establishes is the shared picture of an interfacial/excess sink that fills first and of bulk dissolution that follows only at higher loadings, now supported by two independent experimental readings and by the simulation. The spatial thickness of the plasticized interphase — which neither the 5.8-nm boxes nor the macroscopic probes resolve — remains the open element.

Relative-offset strategy and force-field outlook

The single simulated glass transition of the blend (Section 3.2) traces to the compressed, inverted T_g gap of the present PBAT parameterization (PBAT above PLA), and all quantitative statements above are framed as shift-invariant observables — partition fractions, RDF enrichment ratios, and free-volume invariants — which do not depend on the absolute glass points. The Track-B DFT torsion scans (Section 2.3) were designed to close this gap; their staged application (coarse scans first, gated reparameterization) ended with the adoption gate closing on the transferred-parameter branch (19 K recovered in the quick screen; assuming the recovery transfers to the strict slow-cooling protocol, the excess over experiment would narrow from +101 K to $\approx$ +82 K, Section 3.1), which converts the open parameterization question into a closed diagnosis: the excess is a property of the packing/free-volume equation of state of the transferred nonbonded set. The χ estimates of Section 3.3 bracket the miscibility window from both sides. Within these limits, the miscibility window found here (Flory–Huggins χ straddling zero between the Hildebrand and mixing-energy routes) is consistent with the partial miscibility seen experimentally at 70/30 and with the predicted spinodal instability near 30 vol% PBAT at 296 K for $M_n \approx 30$ kg/mol chains [32].

Limitations and outlook

The principal approximations are the oligomeric chain lengths (PLA-40, PBAT-17, graft PLA-20), the assumed ecoflex-class BT/BA ratio (44/56 mol%; the TH801T copolymer ratio was not characterized), one graft site per chain at a grafting density above the supplier-stated 1.2% (Section 2.1), a single simulated compatibilizer loading (5 phr; the 3 phr and over-dosage regimes are untested), the finite 5.8-nm box ($\approx 2R_g$, so periodic self-image interactions are not fully eliminated), the 3.3×10^9–2.5×10^{10} K/s cooling rates, and the pre-formed graft chemistry; crystallinity and thermal degradation lie outside the classical scope. Two-phase slab simulations of the interfacial tension remained statistically unresolved at accessible box sizes and trajectory lengths, so the interfacial claims of this paper rest on the seed-robust localization observables of Section 3.5. This validated interfacial picture is the entry point for the follow-up foaming studies of this programme, which inherit the free-volume and interfacial descriptors quantified here.

Conclusions

(i) MAH-g-PLA acts as a polymeric surfactant in PLA/PBAT 70/30: the succinic-anhydride graft ring anchors on PBAT-rich domains (1.2–4.6× RDF enrichment across velocity seeds; 74–77% of ring atoms within 0.5 nm of PBAT versus 12–39% for the PLA backbone) while the PLA arm bridges across the interface, enriched 1.13× towards PBAT over pure PLA chains, providing the atomistic counterpart of the 3–5 phr mechanical optima. (ii) ATBC partitions to the compatibilizer-decorated interface and to PBAT-rich regions, with direct PLA-phase dissolution remaining $\leq$7.1% of molecules up to 3.9 phr and doubling to 12.7% only at 5.1 phr ($\leq$13% of

molecules overall) — a picture independently corroborated on the experimental side by the Fox-equation mass balance of the DMA peak shifts, which places ≈98% of the added ATBC outside either phase bulk at 1 phr and 46–52% at 4–5 phr. (iii) At 1–3 phr ATBC anti-plasticizes by free-volume occupation (FFV constant at the two lowest simulated loadings, 1.2 and 2.1 phr, to within ±0.15 percentage points across seeds, rising by only +0.1–0.2 percentage points at 3.9 and 5.1 phr where PLA-phase dissolution grows), the structural signature of the experimental ductility minimum; the corresponding transition-temperature shift lies below the resolving power of the present cooling protocol. (iv) The PBAT glass-transition excess is packing-controlled rather than parametric: a pre-registered first-principles reparameterization gate (DFT fragment charges plus coarse torsion fits) recovers only 19 K of the 101 K excess and closes on the transferred-parameter branch; assuming the 19 K recovery transfers to the strict slow-cooling protocol, the excess over experiment would narrow from +101 K to ≈ +82 K. (v) Together with the χ-bracketed partial miscibility, these shift-invariant descriptors constitute a mechanistic, experimentally anchored foundation for compatibilized/plasticized PLA/PBAT formulation and for the CO_2-foaming studies to follow.

Acknowledgements. The numerical calculations in this paper have been done on the supercomputing system in the High Performance Computing Center of Southwest Petroleum University.

Declarations

Funding. This research did not receive any specific grant from funding agencies in the public, commercial, or not-for-profit sectors.

Competing interests. The authors declare no competing interests.

Data availability. Simulation inputs (mdp files, topologies, force-field patches, and all analysis scripts) and the parsed experimental master tables are deposited in Zenodo [20] (https://doi.org/10.5281/zenodo.22855792); trajectory files are archived on the computing cluster and available on request.

Author contributions. Hongtao Li: Investigation (experiments), Data curation, Writing – review & editing. Lishan Kang: Investigation (experiments), Data curation, Writing – original draft. Letian Shi: Investigation (simulation), Visualization. Ni Tang: Investigation (experiments), Visualization. Mingjun Yang: Conceptualization, Methodology, Software, Supervision, Writing – review & editing.

References

[1] Abraham MJ, Murtola T, Schulz R, et al (2015) GROMACS: High performance molecular simulations through multi-level parallelism from laptops to supercomputers. SoftwareX 1-2:19–25. https://doi.org/10.1016/j.softx.2015.06.001

[2] Aliotta L, Canesi I, Lazzeri A (2021) Study on the preferential distribution of acetyl tributyl citrate in poly(lactic) acid-poly(butylene adipate-co-terephthalate) blends. Polym Test 98:107163. https://doi.org/10.1016/j.polymertesting.2021.107163

[3] Breneman CM, Wiberg KB (1990) Determining atom-centered monopoles from molecular electrostatic potentials. The need for high sampling density in formamide conformational analysis. J Comput Chem 11(3):361–373. https://doi.org/10.1002/jcc.540110311

[4] Bussi G, Donadio D, Parrinello M (2007) Canonical sampling through velocity rescaling. J Chem Phys 126(1):014101. https://doi.org/10.1063/1.2408420

[5] Caputo P, Calandra P, Pecchia A, et al (2024) Reinforcement of polylactic acid / poly butylene adipate-co-terephthalate blends by starch addition: A coupled computational and experimental study. Colloids Surf A Physicochem Eng Asp 685:133159. https://doi.org/10.1016/j.colsurfa.2024.133159

[6] Carmona Esteva FJ, Zhang Y, Maginn EJ, et al (2024) Consistent and reproducible computation of the glass transition temperature from molecular dynamics simulations. J Chem Phys 161(1):014108. https://doi.org/10.1063/5.0207835

[7] Chen RY, Zhang FP, Liu X, et al (2025) Preparation and properties of super toughened PLA/PBAT blends via reactive blending with POE-g-MAH and multifunctional epoxy chain extender. Mater Today Commun 49:113783. https://doi.org/10.1016/j.mtcomm.2025.113783

[8] Chow TS (1980) Molecular interpretation of the glass transition temperature of polymer-diluent systems. Macromolecules 13(2):362–364. https://doi.org/10.1021/ma60074a029

[9] Coltelli MB, Della Maggiore I, Bertoldo M, et al (2008) Poly(lactic acid) properties as a consequence of poly(butylene adipate-co-terephthalate) blending and acetyl tributyl citrate plasticization. J Appl Polym Sci 110(2):1250–1262. https://doi.org/10.1002/app.28512

[10] Fischer EW, Sterzel HJ, Wegner G (1973) Investigation of the structure of solution grown crystals of lactide copolymers by means of chemical reactions. Kolloid-Z Z Polym 251(11):980–990. https://doi.org/10.1007/bf01498927

[11] Fox TG, Flory PJ (1950) Second-order transition temperatures and related properties of polystyrene. I. Influence of molecular weight. J Appl Phys 21(6):581–591. https://doi.org/10.1063/1.1699711

[12] Fredrickson GH, Liu AJ, Bates FS (1994) Entropic corrections to the Flory-Huggins theory of polymer blends: Architectural and conformational effects. Macromolecules 27(9):2503–2511. https://doi.org/10.1021/ma00087a019

[13] Grimme S, Antony J, Ehrlich S, et al (2010) A consistent and accurate *ab initio* parametrization of density functional dispersion correction (DFT-D) for the 94 elements H-Pu. J Chem Phys 132(15):154104. https://doi.org/10.1063/1.3382344

[14] Huang J, Jin B, Zhang X, et al (2024) High energy absorption efficiency and biodegradable polymer based microcellular materials via environmental-friendly CO2 foaming for disposable cushioning packaging. Polymer 292:126612. https://doi.org/10.1016/j.polymer.2023.126612

[15] Jeong S (2023) Investigation of intrinsic characteristics of polymer blends via molecular simulation: a review. Korea-Aust Rheol J 35(4):249–266. https://doi.org/10.1007/s13367-023-00076-9

[16] Jorgensen WL, Maxwell DS, Tirado-Rives J (1996) Development and testing of the OPLS all-atom force field on conformational energetics and properties of organic liquids. J Am Chem Soc 118(45):11225–11236. https://doi.org/10.1021/ja9621760

[17] Kozuch D, Zhang W, Milner S (2016) Predicting the Flory-Huggins χ parameter for polymers with stiffness mismatch from molecular dynamics simulations. Polymers 8(6):241. https://doi.org/10.3390/polym8060241

[18] Kresse G, Furthmüller J (1996) Efficiency of ab-initio total energy calculations for metals and semiconductors using a plane-wave basis set. Comput Mater Sci 6(1):15–50. https://doi.org/10.1016/0927-0256(96)00008-0

[19] Kresse G, Furthmüller J (1996) Efficient iterative schemes for *ab initio* total-energy calculations using a plane-wave basis set. Phys Rev B 54(16):11169–11186. https://doi.org/10.1103/physrevb.54.11169

[20] Li H, Kang L, Shi L, et al (2026) Data deposit: MAH-g-PLA compatibilization and ATBC plasticization of biodegradable PLA/PBAT blends. https://doi.org/10.5281/zenodo.22855792, URL https://doi.org/10.5281/zenodo.22855792, [dataset]

[21] Li X, Qin Y, Li H, et al (2023) Investigating the miscibility of poly (butylene adipate-co-terephthalate)/poly (lactic acid) mixtures through multi-scale simulation and experiments. Macromol Res 31(9):883–896. https://doi.org/10.1007/s13233-023-00172-3

[22] Martínez L, Andrade R, Birgin EG, et al (2009) PACKMOL: A package for building initial configurations for molecular dynamics simulations. J Comput Chem 30(13):2157–2164. https://doi.org/10.1002/jcc.21224

[23] McAliley JH, Bruce DA (2011) Development of force field parameters for molecular simulation of polylactide. J Chem Theory Comput 7(11):3756–3767. https://doi.org/10.1021/ct200251x

[24] Nam K, Kim SG, Kim DY, et al (2024) Enhanced mechanical properties of polylactic acid/poly(butylene adipate-co-terephthalate) modified with maleic anhydride. Polymers 16(4):518. https://doi.org/10.3390/polym16040518

[25] Ostrowska J, Sadurski W, Paluch M, et al (2024) PLA/PBAT blends for blown film extrusion. Polimery 69(7-8):420–429. https://doi.org/10.14314/polimery.2024.7.4

[26] Parrinello M, Rahman A (1981) Polymorphic transitions in single crystals: A new molecular dynamics method. J Appl Phys 52(12):7182–7190. https://doi.org/10.1063/1.328693

[27] Perdew JP, Burke K, Ernzerhof M (1996) Generalized gradient approximation made simple. Phys Rev Lett 77(18):3865–3868. https://doi.org/10.1103/physrevlett.77.3865

[28] Pluhackova K, Morhenn H, Lautner L, et al (2015) Extension of the LOPLS-AA force field for alcohols, esters, and monoolein bilayers and its validation by neutron scattering experiments. J Phys Chem B 119(49):15287–15299. https://doi.org/10.1021/acs.jpcb.5b08569

[29] Prasitnok O, Prasitnok K (2023) Molecular dynamics simulations of copolymer compatibilizers for polylactide/poly(butylene succinate) blends. Phys Chem Chem Phys 25(7):5619–5626. https://doi.org/10.1039/d2cp04765a

[30] Robertson MJ, Tirado-Rives J, Jorgensen WL (2015) Improved peptide and protein torsional energetics with the OPLS-AA force field. J Chem Theory Comput 11(7):3499–3509. https://doi.org/10.1021/acs.jctc.5b00356

[31] Shanu K, Kumar A (2026) Molecular dynamics simulation of gas diffusion in poly(lactic acid)/poly(butylene adipate-co-terephthalate) blends. Mater Chem Phys 359:132535. https://doi.org/10.1016/j.matchemphys.2026.132535

[32] Su S (2021) Prediction of the miscibility of PBAT/PLA blends. Polymers 13(14):2339. https://doi.org/10.3390/polym13142339

[33] Su S, Duhme M, Kopitzky R (2020) Uncompatibilized PBAT/PLA blends: Manufacturability, miscibility and properties. Materials 13(21):4897. https://doi.org/10.3390/ma13214897

[34] Venetsanos F, Anogiannakis SD, Theodorou DN (2022) Mixing thermodynamics and Flory-Huggins interaction parameter of polyethylene oxide/polyethylene oligomeric blends from Kirkwood-Buff theory and molecular simulations. Macromolecules 55(11):4852–4862. https://doi.org/10.1021/acs.macromol.2c00642

[35] Widom B (1963) Some topics in the theory of fluids. J Chem Phys 39(11):2808–2812. https://doi.org/10.1063/1.1734110

[36] Wu Y, Wang C, Xie M, et al (2024) Polybutylene adipate terephthalate/polylactic acid interface enhanced compatibilization and its bead-foaming characteristics. Int J Biol Macromol 279:135221. https://doi.org/10.1016/j.ijbiomac.2024.135221

[37] Xu Y, Meng X, You X, et al (2025) Impact-resistant PLLA/PBAT composites based on novel biobased reactive microcross-linked PBAT. Ind Eng Chem Res 64(3):1623–1634. https://doi.org/10.1021/acs.iecr.4c04307

[38] Yang Q, Ding Y, Liu H, et al (2025) Preparation of PBAT/PLA blend microporous foam with excellent resilience and cushioning properties by scCO2 technology through improving compatibility. J Appl Polym Sci 142(9):e56542. https://doi.org/10.1002/app.56542

[39] Zakizadeh M, Jalali-Aarani A, Garmabi H (2025) Experimental investigation and molecular dynamic simulation of in-situ compatibilization of biodegradable PLA/PBAT blend as a shape memory material. J Polym Environ 33(11):4713–4728. https://doi.org/10.1007/s10924-025-03677-3

[40] Zhang H, Cao J, Jiang L, et al (2026) Block polymer PBAT-b-PLA: A synergistic integration of PLA and PBAT with adjustable structure and properties. Polymer 350:129779. https://doi.org/10.1016/j.polymer.2026.129779